Cell wall integrity and elicitor peptide signaling modulate antimicrobial defense in Arabidopsis via jasmonic acid

Richard Noi Morton[1], Lian Fleischberger[1], Joy Debnath[2], David Biermann[3], Susanne Mühlbauer[4], Ahalya Rajendran[1,#], Hans-Henning Kunz[4], Julien Gronnier[3], Nora Gigli Bisceglia[2] and Timo Engelsdorf[1]*

[1]Molecular Plant Physiology, Department of Biology, Philipps-Universität Marburg, Marburg, Germany
[2]Plant Stress Resilience, Institute of Environmental Biology, Utrecht University, Utrecht, Netherlands
[3]Plant Cell Biology, TUM School of Life Sciences, Technical University of Munich, Freising, Germany
[4]Plant Biochemistry, Department Biology, LMU Munich, Planegg-Martinsried, Germany
[#]present address: Department of Biochemistry, Max Planck Institute for Chemical Ecology, Jena, Germany.

*Corresponding author: Email: timo.engelsdorf@uni-marburg.de

Summary

Cell walls provide mechanical support to plant cells during development and upon exposure to stress. Cell wall integrity (CWI) is monitored by plasma membrane-localized proteins, of which the receptor kinase THESEUS1 (THE1) has been identified as a key CWI sensor in Arabidopsis. THE1-dependent CWI signaling contributes to pathogen resistance, but the underlying mechanism is largely unknown. We report that THE1 loss-of-function mutant plants exhibited increased susceptibility to the cell wall-penetrating fungal pathogen *Colletotrichum higginsianum*, which was associated with reduced synthesis of the antimicrobial metabolite camalexin. Cell wall damage (CWD) caused by cellulose biosynthesis inhibition was sufficient to induce camalexin accumulation in a THE1-, WRKY33-, MPK3- and calcium-dependent manner. Based on our previous finding of coordinated CWI and plant elicitor peptide (Pep) signaling, we investigated the interaction of both pathways for camalexin accumulation. Pep3 treatment caused strong suppression of CWD-induced camalexin biosynthesis downstream of THE1 without affecting *WRKY33* expression. Using RNA-Sequencing and mutant analyses, we discovered four transcription factors that were induced by CWD in a jasmonic acid (JA)-dependent manner and were under negative regulation by Pep3 signaling. We identify MYB47 as a positive regulator of camalexin biosynthesis, activated by THE1 and JA upon CWD, but suppressed by Pep3 through its inhibition of the CWD-induced JA pathway. These data show that CWI signaling is important to activate antimicrobial defense via camalexin, while the negative regulation of CWD responses by Pep3 signaling may represent a mechanism to deactivate local defense at pathogen infection sites when damage prevails.

Key words

Cell wall integrity, pathogen resistance, receptor kinase, protein nanodomains, camalexin, jasmonic acid, plant elicitor peptides, calcium signaling, isoxaben, *Arabidopsis thaliana*

Introduction

Plant cell walls represent sturdy, yet highly dynamic barriers against plant pathogen infection. The ability of pathogens to modify host cell wall properties and to locally breach the barrier determines their successful entry into host tissues and their virulence on specific host plants (Munzert and Engelsdorf, 2025). Consequently, alterations in cell wall composition and structure influence the outcome of plant-pathogen interactions (Molina et al., 2021). It is well established that immune signaling contributes to altered pathogen resistance in cell wall mutants (Bacete et al., 2018) and accumulating evidence suggests that signaling pathways induced by cell wall damage (CWD) contribute to pathogen defense (Vaahtera et al., 2019). The cell wall status is constantly surveilled by a number of overlapping processes together referred to as cell wall signaling (Wolf, 2022). Receptor kinases of the *Catharanthus roseus* receptor-like kinase 1-like (*Cr*RLK1L) family have a prominent role in cell wall signaling during development, growth, damage and immunity (Franck et al., 2018; Ortiz-Morea et al., 2022; Wolf, 2022). *Cr*RLK1Ls are receptors for peptides of the RAPID ALKALINIZATION FACTOR (RALF) family, which are central regulators of *Cr*RLK1L signaling (Schoenaers and Vissenberg, 2025). The *Cr*RLK1L THESEUS1 (THE1) is required for the induction of responses to cell wall damage (CWD), e.g. in cellulose-deficient mutants, after cellulose biosynthesis inhibition with isoxaben (ISX) or after enzymatic cell wall degradation (Hématy et al., 2007; Engelsdorf et al., 2018; Bacete et al., 2022). Binding of RALF34 to THE1 contributes to regulation of lateral root initiation but is dispensable for THE1-dependent responses to ISX (Gonneau et al., 2018). Signaling responses induced by CWD are referred to as cell wall integrity (CWI) signaling (Vaahtera et al., 2019; Wolf, 2022). Responses to ISX include the reactive oxygen species (ROS)- and calcium-dependent induction of phytohormone production and ectopic cell wall lignification (Hamann et al., 2009; Denness et al., 2011). These responses depend on THE1 and the receptor kinase MALE DISCOVERER 1-INTERACTING RECEPTOR LIKE KINASE 2 (MIK2), which have partially overlapping functions in CWI signaling and both contribute to defense against the soilborne fungus *Fusarium oxysporum* (Van der Does et al., 2017). MIK2 is the receptor for SERINE-RICH ENDOGENOUS PEPTIDEs (SCOOPs) that regulate immunity and senescence (Hou et al., 2021; Rhodes et al., 2021; Zhang et al., 2024). ISX-induced CWD promotes SCOOP expression in a partially THE1-dependent manner, which increases responses to a subsequent treatment with pathogen-associated molecular patterns (PAMPs) (Zhai et al., 2024). This highlights how signals originating from a damaged cell wall can contribute to pattern-triggered immunity (PTI).

Intriguingly, loss of PTI elements such as BRASSINOSTEROID INSENSITIVE 1 (BRI1)–ASSOCIATED KINASE 1 (BAK1), BAK1-LIKE 1 (BKK1), BOTRYTIS-INDUCED KINASE 1 (BIK1), PEP1 RECEPTOR 1 (PEPR1) and PEPR2 leads to increased ISX responses, indicating that PTI can negatively regulate CWI signaling (Engelsdorf et al., 2018). This (feedback) inhibition exerted by PTI on CWI signaling depends on endogenous plant elicitor peptides (Peps) that are perceived by PEPR1/2 and BAK1 (Yamaguchi et al., 2006; Yamaguchi et al., 2010; Tang et al., 2015). Pep1 and Pep3 precursor genes, *PROPEP1* and *PROPEP3*, are induced in a THE1-independent manner after 1 hour of ISX treatment and co-treatment of seedlings with ISX and synthetic Pep1 or Pep3 suppresses ISX-induced accumulation of the phytohormones jasmonic acid (JA) and salicylic acid (SA) (Engelsdorf et al., 2018). *PROPEPs* are also induced by wounding, salinity, pathogen infection or PAMP treatments, but the direct stimulus leading to their expression is unknown (Bartels and Boller, 2015; Nakaminami et al., 2018). Overexpression of *PROPEP1* and *PROPEP3* is sufficient to rescue plants from cell death after long-term treatment with ISX or growth under high salinity, demonstrating their impact on stress resistance (Nakaminami et al., 2018; Zhang et al., 2025). Cellular damage activates calcium-, SUMOylation- and metacaspase-dependent PROPEP processing and released Peps can spread danger signals to neighboring cells (Hander et al., 2019; Shen et al., 2019; Zhang et al., 2025).

Recognition of pathogens induces the production of phytohormones and of specialized antimicrobial metabolites, termed phytoalexins (Ahuja et al., 2012). In Arabidopsis, the major phytoalexin camalexin is synthesized by a metabolon comprising several Cytochrome P450 enzymes, whose expression is regulated by WRKY transcription factors (Birkenbihl et al., 2012; Birkenbihl et al., 2017; Mucha et al., 2019). WRKY33, the major positive regulator of camalexin biosynthesis, is induced in response to pathogen infection by MAP kinase (MPK)- and calcium-induced phosphorylation and is important for efficient defense against fungal pathogens (Zheng et al., 2006; Mao et al., 2011; Schmidt et al., 2020; Zhou et al., 2020). During fungal infections, camalexin is produced locally at infection sites and secreted by the transporters PLEITROPIC DRUG RESISTANCE 8 (PDR8/PENETRATION3) and PDR12 (Glawischnig, 2007; He et al., 2019).

In summary, the state of the art suggests that THE1-dependent CWI monitoring can contribute to basal defense against pathogen infection. Here, we explored how camalexin biosynthesis is activated and regulated upon CWD and how negative regulation by Pep3 is implemented in this defense mechanism.

Results

THE1 contributes to camalexin accumulation and pathogen resistance

We investigated if THE1 contributes to penetration resistance to the hemibiotrophic fungus *Colletotrichum higginsianum*, which depends on host cell wall penetration, causing local CWD (O'Connell et al., 2004; Engelsdorf et al., 2017). The *the1-1* loss of function allele displayed a higher *C. higginsianum* entry rate, which was accompanied by reduced accumulation of the major Arabidopsis phytoalexin camalexin, indicating that THE1 might contribute to induction of camalexin biosynthesis upon fungal infection (Figure 1A,B). To estimate the contribution of impaired camalexin accumulation to *the1-1* susceptibility, we crossed *the1-1* with the camalexin-deficient *pad3* mutant and quantified fungal genomic DNA at 4 days post infection (dpi). Fungal DNA was significantly increased in *the1-1*, *pad3* and *the1-1 pad3* compared to WT, but not significantly different between single and double mutants, indicating overlapping effects of THE1 and camalexin synthesis on pathogen resistance (Figure 1C).

Cell wall damage is sufficient to induce THE1-dependent camalexin accumulation

The finding that THE1 played a role in camalexin induction upon pathogen infection prompted us to investigate if CWI impairment is sufficient to induce camalexin biosynthesis. We examined the transcriptional regulation of camalexin biosynthesis genes after ISX treatment in a publicly available transcriptomics dataset (Hamann et al., 2009) and found strong upregulation of the camalexin pathway (Figure S1). ISX treatments are ideally suited to further investigate the regulation of CWD-induced camalexin biosynthesis, as treatments can be performed in seedling liquid culture in a controlled and well-established manner separating CWD from other molecular events that occur during plant-pathogen interactions (Hamann et al., 2009; Denness et al., 2011; Wormit et al., 2012; Van der Does et al., 2017; Engelsdorf et al., 2018; Gigli-Bisceglia et al., 2018; Engelsdorf et al., 2019; Chaudhary et al., 2020; Chaudhary et al., 2021; Bacete et al., 2022; Zhai et al., 2024). Consistent with transcriptional activation of camalexin biosynthesis, ISX treatments of 10 days old seedlings induced camalexin accumulation after 8 hours (Figure 2A). We have previously shown that treatment of Arabidopsis seedlings with Driselase, a mixture of cell wall-degrading enzymes, induces similar CWI responses as ISX treatment (Engelsdorf et al., 2018). In line with that, camalexin accumulation was increased after Driselase treatment compared to heat-inactivated Driselase, indicating that camalexin accumulation is induced by different types of CWD (Figure S2). Stress-induced conversion of the key indolic intermediate indole-3-acetaldoxime (IAOx) to indole-3- acetonitrile (IAN) for camalexin biosynthesis depends on the two cytochrome P450 enzymes CYP71A12 and CYP71A13, with stronger contribution of the latter (Müller et al., 2015). Transcriptional data indicated that *CYP71A12* was already induced after 4 hours ISX

150 treatment, whereas *CYP71A13* was upregulated 8 hours after ISX treatment, following a
151 similar expression pattern as *CYP71B15/PAD3*, the final enzyme in camalexin biosynthesis
152 (Figure S1). Loss of CYP71A13 completely abolished ISX-induced camalexin accumulation,
153 while loss of CYP71A12 increased camalexin accumulation (Figure 2B). This data shows that
154 CYP71A13 is essential for ISX-induced camalexin biosynthesis, whereas CYP71A12 rather
155 diverges IAOx for other pathways such as indole-3-carboxylic acid (ICA) synthesis (Pastorczyk
156 et al., 2020). To investigate if CWD-induced camalexin biosynthesis depends on THE1, we
157 quantified camalexin in ISX-treated *the1-1* seedlings and found that camalexin accumulation
158 was completely abolished in the mutant (Figure 2C). Instead, treatment of the hypermorphic
159 *the1-4* allele (Merz et al., 2017) caused increased camalexin accumulation (Figure 2C).
160 Camalexin accumulation was abolished in an ISX-treated *wrky33* mutant and close to the
161 detection limit in *the1-4 wrky33* double mutants, showing that the major transcriptional
162 regulator of camalexin biosynthesis, WRKY33, is necessary for ISX-induced, THE1-dependent
163 camalexin synthesis (Figure 2D).
164
165 **Calcium signaling determines the magnitude of ISX-induced camalexin response**
166 Previous studies demonstrated that Ca^{2+} signaling was required for ISX-induced JA
167 accumulation (Denness et al., 2011) and that Ca^{2+} transients were involved in CWI
168 maintenance under high salinity (Feng et al., 2018). Consistently, blocking of calcium channels
169 with $LaCl_3$ during ISX treatments indicated that Ca^{2+} signaling was required for ISX-induced
170 camalexin accumulation (Figure 2E). To better understand which channels and Ca^{2+} sensing
171 mechanisms contribute to this response, we investigated mutants for the plasma membrane
172 localized channel MATING PHEROMONE INDUCED DEATH 1 (MID1)–COMPLEMENTING
173 ACTIVITY 1 (MCA1), which has been previously implicated in mechanosensing and CWI
174 signaling (Nakagawa et al., 2007; Engelsdorf et al., 2018), and the chloroplast localized
175 CALCIUM SENSING RECEPTOR (CAS), which is required for the regulation of cytosolic Ca^{2+}
176 transients upon external Ca^{2+} signals (Nomura et al., 2008; Weinl et al., 2008). Camalexin
177 accumulation in response to ISX treatment was reduced by 60 and 47 % in *cas* and *mca1*
178 mutants, respectively, supporting that both genes contribute to CWD responses (Figure 2F).
179 Stress induced Ca^{2+} transients occur in the cytosol and in the chloroplast stroma (Nomura et
180 al., 2012). To test whether altered distribution between stromal and cytosolic Ca^{2+} influences
181 ISX responses, we investigated camalexin production in double mutants of the PLASTID
182 ENVELOPE ION CHANNELs (PEC1, PEC2) that exhibit reduced stromal and increased
183 cytosolic Ca^{2+} transients after stress exposure (Völkner et al., 2021). ISX treatment induced
184 higher camalexin accumulation in *pec1 pec2* than in the WT, indicating that increased cytosolic
185 Ca^{2+} strengthens the CWD response (Figure 2G). The importance of Ca^{2+} at a later stage
186 (hours) of CWD might indicate that Ca^{2+} signaling is influenced by CWI status. To test this idea,

187 we elicited Ca^{2+} transients in WT and *pec1 pec2* seedlings after mock and ISX treatment and
188 quantified cytosolic Ca^{2+}. The results show that cytosolic Ca^{2+} was increased upon elicitation
189 with high salinity in ISX- compared to mock-treated seedlings, indicating that CWD increases
190 the sensitivity for Ca^{2+} elicitation with another cell wall stress-inducing stimulus (Figure 2H,I).
191
192 **Pep3-triggered signaling inhibits CWI signaling downstream of THE1**
193 We have previously reported that ISX-induced, THE1-dependent phytohormone responses are
194 negatively regulated by Pep1 and Pep3, but the underlying mechanism remained unknown
195 (Engelsdorf et al., 2018). To investigate how Pep perception affects ISX-induced camalexin
196 accumulation, we treated Col-0, *pepr1 pepr2* and *bak1-5 bkk1* seedlings with ISX, Pep3 and
197 a combination of both. We chose Pep3 for this study, (i) because it suppresses THE1-
198 dependent phytohormone accumulation, but, unlike Pep1, does not induce ectopic root
199 lignification, and (ii) because we previously demonstrated that PROPEP3 is secreted upon cell
200 wall damage (Engelsdorf et al., 2018). Pep3 co-treatment led to suppression of ISX-induced
201 camalexin accumulation in a PEPR- and BAK1/BKK1-dependent manner (Figure 3A),
202 indicating that Pep3 inhibits THE1-dependent camalexin synthesis via PEPR-mediated
203 signaling.
204 Despite of the recognized function of THE1 as a CWI sensor, little is known about its regulation
205 upon perception of CWD. Accumulating reports link changes in the plasma membrane protein
206 organization and initiation of cell signaling (Jaillais et al., 2024). We combined enhanced super-
207 resolution radial fluctuation (eSRRF) (Laine et al., 2023) with variable-angle total internal
208 reflection microscopy (VA-TIRFM) imaging (Konopka and Bednarek, 2008) to analyze the
209 plasma membrane organization of THE1-GFP upon CWD. We observed that a subpopulation
210 of THE1-GFP was organized into nanodomains and that 1 hour and 6 hours of ISX treatment
211 led to a decrease in the density of THE1-GFP nanodomains (Figure 3B,C). Congruently, the
212 relative proportion of THE1-GFP localization within nanodomains and the image-wide spatial
213 clustering index (iSCI) of THE1-GFP were reduced at both time points after ISX treatment
214 (Figure S3). Confocal microscopy showed that THE1-GFP localization to the plasma
215 membrane was unaffected by ISX treatment (Figure S4). Together, these data indicate that
216 THE1-GFP is spatially redistributed within the plasma membrane upon CWD induced by ISX
217 and may indicate that THE1-GFP nanodomains correspond to resting pools of the receptor
218 that are released for function. To test whether the inhibition of THE1-mediated camalexin
219 synthesis could be linked to an effect of Pep3 on ISX-triggered changes in THE1 localization,
220 we treated THE1-GFP seedlings with ISX, Pep3 and a combination of both. Neither the mean
221 THE1-GFP fluorescence at the plasma membrane nor THE1 nanodomain organization were
222 altered by Pep3 co-treatment, suggesting that negative regulation of ISX responses is exerted
223 downstream of THE1 (Figure 3B,C, Figure S3, Figure S4). In good agreement with this

224 conclusion, suppression of ISX-induced camalexin by Pep3 was observed in the hypermorphic
225 *the1-4* allele (Figure 3D).
226
227 **Pep3-dependent inhibition of CWI responses is independent from WRKY33 and MPK3/6**
228 To investigate if Pep3 inhibition of THE1 signaling involves transcriptional regulation of
229 *WRKY33* or *PAD3*, we performed time course qRT-PCR analysis in Col-0, *the1-1*, *the1-4* and
230 *pepr1 pepr2* mutants. Pep3 treatment led to upregulation of *WRKY33* after 2 hours, whereas
231 *PAD3* expression was not induced at this time point (Figure S5). ISX caused the upregulation
232 of *WRKY33* between 2 and 4 hours after treatment and of *PAD3* between 4 and 6 hours after
233 treatment (Figure S5). Notably, ISX-induced *WRKY33* induction was neither significantly
234 affected by THE1, nor by Pep3 co-treatment (Figure 4A). Instead, *PAD3* induction after ISX
235 treatment was reduced in *the1-1,* increased in *the1-4* and suppressed by Pep3 co-treatment,
236 showing that THE1 and Pep3 regulate *PAD3* without influencing *WRKY33* expression (Figure
237 4B).
238 We previously reported that the MAP kinase kinase kinase (MAPKKK) family proteins
239 Arabidopsis NPK1-related Protein kinase 1 (ANP1) and ANP3 regulate ISX-dependent
240 responses, indicating that MPK signaling plays a role in CWI signaling (Gigli Bisceglia et al.,
241 2018). Camalexin accumulation after pathogen infection involves phosphorylation of WRKY33
242 by MPK3 and MPK6, both of which are phosphorylated by Pep3-triggered signaling (Mao et
243 al., 2011; Bartels et al., 2013). To test if MPK3/6 are involved in ISX-induced camalexin
244 synthesis and/or in Pep3-dependent inhibition of the same, we analyzed camalexin levels in
245 Col-0, *mpk3* and *mpk6* seedlings after treatment with mock, Pep3, ISX and ISX+Pep3. MPK3,
246 but not MPK6, was required for ISX-induced camalexin accumulation (Figure 4C). We were
247 however unable to detect any changes in MPK3/6 phosphorylation after ISX treatment for 10
248 min, when CESAs are internalized (Paredez et al., 2006), as well as after 4 and 6 hours, when
249 transcriptional responses become more pronounced and phytohormones and camalexin start
250 to accumulate (Denness et al., 2011; Engelsdorf et al., 2018; Zhai et al., 2024) (Figure S6).
251 While Pep3 single or combined treatments induced MPK3 and MPK6 phosphorylation (Figure
252 S6), Pep3-dependent suppression of ISX-induced camalexin accumulation was not affected in
253 *mpk3* and *mpk6* mutants, suggesting that MPK3/6 signaling is not required for Pep3-triggered
254 inhibition of CWI responses (Figure 4C).
255 Taken together, our data indicate that Pep3-PEPR signaling inhibits ISX-induced production of
256 camalexin downstream of THE1 and independent from MPK3/6 and WRKY33.
257
258 **MYB and WRKY transcription factors are regulated by THE1 and Pep3 signaling**
259 To identify candidate genes that mediate Pep3 inhibition of CWI signaling, we performed RNA-
260 Sequencing of Col-0 seedlings treated with mock, Pep3, ISX and ISX+Pep3 for 6 hours, when

261 *PAD3* expression was suppressed by the co-treatment (Figure 4B). Principal component
262 analysis showed that biological replicates grouped according to treatments and indicated that
263 the largest share of the transcriptional changes in the data sets could be explained by ISX
264 treatment (Figure S7A). Hierarchical cluster analysis supported this conclusion by grouping
265 ISX and ISX+Pep3 treatments together but also revealed groups of genes with opposite
266 expression patterns between both treatments (Figure S7B). Analysis of differential gene
267 expression identified 543 genes significantly downregulated (α=0.05, fold change > 2) after
268 Pep3 (89 genes), ISX (330) and ISX+Pep3 (313) treatment compared to mock control (Figure
269 S7C). Instead, 1513 genes were upregulated (α=0.05, fold change > 2) after treatment with
270 Pep3 (416 genes), ISX (1248) and ISX+Pep3 (1104) (Figure 5A). The transcription factors
271 *MYB47*, *MYB95*, *MYB113* and *WRKY67* were significantly upregulated by ISX, but not after
272 combined ISX+Pep3 treatment, making them candidates for mediating the negative effect of
273 Pep3 on CWI signaling. Quantitative RT-PCR showed that *MYB47*, *MYB95* and *MYB113* were
274 induced in a THE1-dependent and WRKY33-independent manner (Figure 5B-D), while
275 *WRKY67* expression depended on THE1 but was negatively regulated by WRKY33 (Figure
276 5E). To investigate if MYB47 and the closely related MYB95 (Millard et al., 2019) are involved
277 in the regulation of ISX-dependent camalexin accumulation by Pep3, we subjected *myb47*
278 single and *myb47/95* double mutants to mock, Pep3, ISX and combined ISX and Pep3
279 treatments. We detected significantly reduced camalexin levels after ISX treatment in both
280 lines, indicating that MYB47 is required for induction of camalexin biosynthesis, whereas loss
281 of MYB95 did not add to the phenotype (Figure 5F,G). Two independent mutant lines for
282 *MYB113* did not cause significant changes in camalexin accumulation compared to WT (Figure
283 5H; Figure S8). We also attempted to obtain independent mutant lines for *WRKY67* but
284 encountered inconsistent seed germination and developmental phenotypes, currently
285 preventing further investigation.
286 Taken together, our RNA-Seq study identified about three times more upregulated than
287 downregulated genes after 6 hours of ISX treatment and among them four transcription factors
288 that were suppressed by Pep3 co-treatment. *MYB47* was induced in a strictly THE1-dependent
289 manner and required for camalexin accumulation after CWD induction by ISX treatment.
290
291 **MYB47 mediates THE1-induced and Pep3-sensitive JA signaling**
292 In line with increased JA levels after ISX treatment (Denness et al., 2011), JA related gene
293 expression was strongly increased 6 hours after ISX treatment (Figure 6A). Instead, genes
294 involved in JA biosynthesis, signaling and catabolism were negatively regulated after Pep3
295 treatment and showed an attenuated expression profile after combined ISX+Pep3 treatment
296 compared to ISX treatment alone (Figure 6A). Recently, JA was also connected to camalexin
297 biosynthesis induction via ERF1B (Zhou et al., 2022) and previous research demonstrated that

298 JA accumulation in response to ISX treatment is sensitive to Pep signaling (Engelsdorf et al.,
299 2018). This overlap prompted us to investigate the role of JA in ISX-induced camalexin
300 production and its Pep3-dependent negative regulation. JA-deficient *aos* mutants did not
301 accumulate camalexin after ISX treatment, supporting an essential role of JA (Figure 6B).
302 Since JA induction after ISX treatment is suppressed by Pep3 (Engelsdorf et al., 2018), we
303 hypothesized that exogenous application of JA might abrogate Pep3-dependent suppression
304 of camalexin production. Indeed, triple treatment with ISX, Pep3 and JA strongly induced
305 camalexin accumulation, demonstrating that JA application is sufficient to override the negative
306 influence of Pep3 (Figure 6C).
307 Next, we investigated if ISX-induced expression of *MYB47*, *MYB95*, *MYB113* and *WRKY67*
308 depended on JA biosynthesis. Quantitative RT-PCR showed that ISX-dependent induction of
309 *MYB47*, *MYB113* and *WRKY67* was abolished and induction of *MYB95* attenuated in JA-
310 deficient *aos* mutants (Figure 6D-G). To clarify if the homologous MYB47 and MYB95
311 transcription factors are involved in the regulation of JA signaling, we investigated expression
312 of the JA marker gene *JAZ10* in *myb47/95* mutants. ISX-induced *JAZ10* expression was not
313 compromised in the mutant, demonstrating that MYB47 and MYB95 influence CWI signaling
314 downstream of JA (Figure 6H). In addition, ERF1B was induced in *myb47/95* mutants like in
315 the WT, placing MYB47 and MYB95 downstream or independent of ERF1B (Figure S9). ISX-
316 induced expression of *WRKY33* was JA- and MYB47/95-independent, further supporting the
317 independent regulation of THE1-JA-MYB47/95 and WRKY33 pathways in camalexin induction
318 (Figure S10).
319
320 **Discussion**
321 In this study, we investigated contributions of THE1-dependent CWI signaling to pathogen
322 defense and its interaction with Pep signaling. We show that CWI impairment is sufficient to
323 induce camalexin accumulation and this response requires both THE1 and WRKY33 (see
324 Figure 6I for a model). In line with the previously described role of WRKY33 as central regulator
325 of camalexin biosynthesis (Mao et al., 2011), increased CWI signaling in the hypermorphic
326 *the1-4* mutant required WRKY33 for camalexin induction. WRKY33 expression was induced
327 by ISX treatment, but was neither dependent on THE1, nor affected by co-treatment with Pep3.
328 This is in contrast with ISX-induced expression of PAD3, catalyzing the final step of camalexin
329 synthesis, which strongly depended on THE1 and was suppressed by co-treatment with Pep3.
330 Phosphorylation by MPK3/6 and CALCIUM-DEPENDENT PROTEIN KINASEs (CPK5/6)
331 controls WRKY33 DNA binding, autoactivation, and transactivation of key camalexin
332 biosynthesis genes (Zhou et al., 2020). Our analysis showed that MPK3 controls ISX-induced
333 camalexin accumulation, while MPK6 was not required. MPK3 phosphorylation was not
334 detectable at 10 minutes, 4 hours and 6 hours after ISX treatment, indicating that (i) MPK

335 phosphorylation after ISX treatment is not a fast response, and (ii) that it may represent a
336 transient and/or dynamic response that is difficult to catch.
337 The importance of calcium signaling for ISX-induced CWD responses has been long
338 recognized (Denness et al., 2011), but the exact mode of action remains elusive. Current
339 evidence suggests that MCA1 might represent a stretch-activated Ca^{2+} channel required for
340 THE1-dependent CWI signaling (Nakagawa et al., 2007; Engelsdorf et al., 2018). Delayed
341 inhibitor treatment assays with $LaCl_3$ showed that calcium signaling affects responses to ISX
342 treatment that occur in the scale of hours, when CWD causes mechanical damage and
343 microscopically visible phenotypes (Denness et al., 2011; Engelsdorf et al., 2018; Bacete et
344 al., 2022). Congruently, $LaCl_3$ treatment abolished ISX-induced camalexin accumulation. Loss
345 of MCA1 halved camalexin levels compared to wild type, indicating that it may be partially
346 responsible for Ca^{2+} influx after CWD. Similarly, CAS, a chloroplast-localized positive regulator
347 of Ca^{2+} responses in the cytosol and the chloroplast stroma (Nomura et al., 2008; Weinl et al.,
348 2008; Nomura et al., 2012), contributed to camalexin accumulation in response to ISX. Instead,
349 loss of chloroplast inner envelope ion channels PEC1/2 impairs stromal Ca^{2+} transients but
350 increases cytosolic Ca^{2+} transients, suggesting that Ca^{2+} is partially excluded from plastids
351 (Völkner et al., 2021). Our data indicate that increased cytosolic Ca^{2+} in *pec1/2* triggered ISX-
352 induced camalexin accumulation. While the *Cr*RLK1L FER contributes to CWI maintenance
353 during high salinity by inducing late Ca^{2+} transients (Feng et al., 2018), *fer* mutants exhibit
354 constitutively increased CWD responses that cannot be alleviated by loss of THE1 (Engelsdorf
355 et al., 2018; Gonneau et al., 2018), indicating that different Ca^{2+} signatures might be involved
356 in CWI maintenance and CWD responses. We provide first hints that CWD increases
357 responsiveness to cell wall-related Ca^{2+} elicitation as ISX treated seedlings responded
358 stronger to high salinity. It will be interesting to investigate in the future if CWI sensors
359 contribute to this response.
360 In recent years, plasma membrane localized proteins have been recognized to be dynamically
361 organized in specific nanodomains according to developmental programs and stress
362 responses (Bücherl et al., 2017; Hdedeh et al., 2025). Protoplast cell wall regeneration assays
363 indicated that the cell wall influences lateral mobility of plasma membrane proteins and
364 chemical treatments affecting cellulose biosynthesis or pectin methylation caused changes in
365 protein nanodomain size and dynamics (Martinière et al., 2012; McKenna et al., 2019). These
366 changes might influence signaling, as the nanodomain organization of RLKs is influenced by
367 FER, cell wall localized LRR-EXTENSIN (LRX) and their ligand RALF23 (Gronnier et al., 2022;
368 Liu et al., 2024). In line with its central function in CWI signaling upon CWD, THE1 was spatially
369 reorganized at the plasma membrane after one hour of ISX treatment, showing that THE1
370 reorganization precedes accumulation of phytohormones and camalexin. This observation
371 suggests that THE1 may be released from nanodomains for function. Similarly, during viral

372 infection, the solicitation of REMORIN proteins correlates with their spatial redistribution and
373 an overall increase in their lateral diffusion (Perraki et al., 2018; Jolivet et al., 2025). Because
374 ligand-induced signaling can influence nanodomain organization of other receptor kinases
375 (Gronnier et al., 2022), we considered the possibility that Pep3 signaling may influence THE1
376 nanodomain organization. However, we observed no effects of Pep3 treatments on THE1-GFP
377 nanodomains under mock or ISX conditions, indicating interaction of CWI and Pep3 pathways
378 downstream of THE1. Consistently, we observed that Pep3 inhibited ISX-induced camalexin
379 accumulation in the hypermorphic *the1-4* allele.
380 To identify potential downstream regulators, we performed transcriptomics and discovered four
381 candidate transcription factors that were induced by ISX treatment in a THE1-dependent
382 manner and suppressed by Pep3 co-treatment, indicating that they are downstream of a Pep3-
383 THE1 pathway interaction. *WRKY67* expression was negatively regulated by WRKY33 after
384 ISX treatment, which may be mediated via interaction with WRKY18/40 (Birkenbihl et al.,
385 2017). *MYB47*, *MYB95* and *MYB113* were not affected in a *wrky33* mutant, making them
386 candidates for THE1-dependent, WRKY33-independent signaling. Mutant analysis revealed
387 that *MYB47* is required for ISX-induced camalexin accumulation, extending the network of
388 transcription factors known to be involved in the regulation of camalexin biosynthesis. MYB34,
389 MYB51 and MYB122 regulate *CYP79B2* and *CYP79B3*, thereby affecting the conversion of
390 tryptophan to IAOx and determining precursor availability for camalexin synthesis (Frerigmann
391 et al., 2015). Instead, ANAC042, ERF1B and ERF72 are required for transcriptional induction
392 of *CYP71A13* and *PAD3*, directly regulating the camalexin biosynthesis pathway (Saga et al.,
393 2012; Li et al., 2021; Zhou et al., 2022; Monsalvo et al., 2025). Of note, ERF1B cooperates
394 with WRKY33 to induce camalexin pathway genes and is induced by JA (Zhou et al., 2022).
395 These properties are reminiscent of THE1 signaling in response to CWD, which induces the
396 JA pathway and acts in parallel to WRKY33 in camalexin synthesis. Indeed, JA was required
397 for ISX-induced camalexin accumulation as well as for induction of *MYB47*, *MYB95*, *MYB113*
398 and *WRKY67.* In Arabidopsis roots, cellulose defects cause cortex cell bulging and
399 compression of inner tissues stimulating JA signaling (Mielke et al., 2021). The same
400 mechanism might be responsible for JA induction after ISX treatment, where THE1 is required
401 for CWD detection. *MYB47* induction was recently reported in drought treated Arabidopsis
402 plants, where it was associated with increased JA signaling and drought stress survival
403 (Marquis et al., 2022). Since drought stress impairs CWI (Novaković et al., 2018), it would be
404 interesting to test if *MYB47* expression upon drought is induced by THE1-dependent CWI
405 signaling. JA treatment alone was not sufficient to induce camalexin synthesis, and the
406 available data indicates that at least two independent pathways need to be activated upon
407 CWD to initiate this defense response. Consistently, negative regulation of JA synthesis by

408 Pep3 treatment was sufficient to suppress the camalexin pathway whereas JA application
409 overrode the suppressive effect of Pep3 on ISX-induced camalexin accumulation.
410 Taken together, perception of CWD involves changes in THE1 nanodomain organization at the
411 plasma membrane and regulation of Ca^{2+} signaling via MCA1, CAS and PEC (Figure 6I).
412 THE1-induced JA signaling and THE1-independent WRKY33 are both induced by CWD and
413 required for camalexin accumulation. Negative regulation of this cell wall-mediated defense
414 response by PEPR-mediated perception of Pep3 is placed upstream of JA. We identified
415 *MYB47*, *MYB95*, *MYB113* and *WRKY67* as ISX-induced, THE1- and JA-dependent
416 transcription factors, of which MYB47 was required for ISX-induced camalexin accumulation.
417 We propose that the induction of camalexin production and secretion by CWD contributes to
418 targeted defense at fungal penetration sites. In turn, current evidence suggests that Peps are
419 released upon plasma membrane rupture allowing their binding to PEPRs of neighboring cells
420 (Hander et al., 2019; Shen et al., 2019). Pep3 detection may therefore signify rampant damage
421 on the tissue level, leading to suppression of local cell wall-mediated defense at infection sites.
422
423 **Materials and Methods**
424 Plant materials and growth conditions
425 *Arabidopsis thaliana* genotypes used in this study are listed in Supplemental Table S1.
426 Accession Columbia-0 (Col-0) was used as wild type in all experiments. All Arabidopsis
427 mutants used in this study were either obtained from the Nottingham Arabidopsis Stock Centre
428 (http://arabidopsis.info/), from laboratories where data on them has been published, or have
429 been crossed from those.
430 For growth in sterile liquid culture, seeds were surface sterilized for 10 minutes with 70% (v/v).
431 The ethanol was subsequently replaced with a sterilizing solution of 2% sodium hypochlorite
432 with 0.1% Triton X-100, treated for additional 3 minutes and finally rinsed four times with sterile
433 water. Seeds were then stratified at 4°C for 3 days before transfer to half-strength Murashige
434 and Skoog liquid medium [Murashige and Skoog Basal Medium (2.1 g/liter), MES salt (0.5
435 g/liter), and 1% sucrose, pH 5.7]. Seedling cultures were established in a 24-well plate with 6
436 seeds per well. Seedlings were grown under a 16-hour light (22°C) / 8-hour dark (20°C) cycle
437 and a photon flux density of 110μmol m^{-2} s^{-1}.
438 For growth on soil, Arabidopsis seeds were placed on a mixture of 80% Fruhstorfer Type P
439 (Hawita, Germany) and 20% Liadrain clay (Liapor, Germany), stratified for 3 days and grown
440 at a photon flux density of 110μmol m^{-2} s^{-1} under the light cycles indicated in the figure legends.
441
442 Plant liquid culture treatments
443 Unless stated otherwise, 10-day-old seedlings were subjected to the following treatments in
444 fresh liquid growth medium at the indicated final concentrations: 600 nM isoxaben (ISX;

445 Supelco 36138), 10 nM *At*Pep3, 600 nM ISX + 10 nM *At*Pep3 (combined treatment of ISX and
446 AtPep3), 10mM $LaCl_3$, 5µM jasmonic acid (JA; Cayman Chemical 88300), 600 nM ISX + 10
447 nM *At*Pep3 + 5µM JA (combined treatment of ISX, *At*Pep3, and JA). Equal amounts of DMSO
448 were present in all treatments, including mock treatments. Treatment with 0.03% (w/v)
449 Driselase (Dri; Sigma-Aldrich D8037) and inactivated (bDri) was performed according to
450 Engelsdorf et al. (2018). After treatment, seedlings were briefly rinsed, patted dry, snap-frozen
451 in liquid nitrogen and stored at -70°C until further analysis. *At*Pep3
452 (EIKARGKNKTKPTPSSGKGGKHN) was custom synthesized and supplied by EZBiolab Inc.
453 (Indiana, USA).
454
455 *Colletotrichum higginsianum* infection assays
456 *Colletotrichum higginsianum* isolate MAFF 305635 (Ministry of Forestry and Fisheries, Japan)
457 was used for all infection experiments. Conidia were plated on oatmeal agar (5% [w/v]
458 shredded oatmeal, 1.2% [w/v] agar) and incubated for 7 days in a 16 h light (22°C) / 8 h dark
459 (20°C) cycle at a photon flux density of 110 µmol m^{-2} s^{-1}. Immediately prior to infection, conidia
460 were harvested by rinsing plates with deionized water and the titer was adjusted to $2 \cdot 10^6$
461 conidia ml^{-1}. Spray infection of leaf rosettes was performed at the end of the light phase and
462 high humidity maintained until 2.5 days post infection to support fungal penetration as
463 described (Voll et al., 2012). Fungal entry rates were determined by microscopic examination
464 after staining fungal structures with trypan blue as described in Engelsdorf et al. (2017) and
465 quantification of the relative fungal DNA content in infected leaves was performed by qPCR
466 analysis of *ChTrpC* as described in Engelsdorf et al. (2013).
467
468 Quantitative reverse transcription polymerase chain reaction (qRT-PCR)
469 Total RNA was isolated using a NucleoSpin Plant and Fungi RNA Mini Kit (Macherey-Nagel).
470 One microgram of total RNA was treated with RNase-Free DNase (Thermo Scientific) and
471 used for complementary DNA (cDNA) synthesis with a RevertUP II Reverse Transcriptase Kit
472 (Biotechrabbit). Quantitative reverse transcription polymerase chain reaction (qRT-PCR) was
473 performed using Blue S'Green (Biozym) SYBR green mix and a Bio-Rad CFX Connect RT-
474 PCR system. Primers are listed in Supplemental Table S2. *ACT2* was used a reference in all
475 experiments.
476
477 RNA-Sequencing
478 Total RNA was isolated using a NucleoSpin Plant and Fungi RNA Mini Kit (Macherey-Nagel)
479 and shipped to Novogene Europe (Cambridge, UK) for further processing. RNA integrity was
480 assessed using the RNA Nano 6000 Assay Kit of the Bioanalyzer 2100 system (Agilent
481 Technologies, CA, USA). Total RNA was used as input material for the RNA sample

482 preparations. Briefly, mRNA was purified from total RNA using poly-T oligo-attached magnetic
483 beads. Fragmentation was carried out using divalent cations under elevated temperature in
484 First Strand Synthesis Reaction Buffer(5X). First strand cDNA was synthesized using random
485 hexamer primer and M-MuLV Reverse Transcriptase (RNase H-). Second strand cDNA
486 synthesis was subsequently performed using DNA Polymerase I and RNase H. Remaining
487 overhangs were converted into blunt ends via exonuclease/polymerase activities. After
488 adenylation of 3' ends of DNA fragments, Adaptor with hairpin loop structure were ligated to
489 prepare for hybridization. In order to select cDNA fragments of preferentially 370~420 bp in
490 length, the library fragments were purified with AMPure XP system (Beckman Coulter, Beverly,
491 USA). Then PCR was performed with Phusion High-Fidelity DNA polymerase, Universal PCR
492 primers and Index (X) Primer. At last, PCR products were purified (AMPure XP system) and
493 library quality was assessed on the Agilent Bioanalyzer 2100 system. The clustering of the
494 index-coded samples was performed on a cBot Cluster Generation System using TruSeq PE
495 Cluster Kit v3-cBot-HS (Illumina) according to the manufacturer's instructions. After cluster
496 generation, the library preparations were sequenced on an Illumina Novaseq platform and 150
497 bp paired-end reads were generated. Raw data (raw reads) of fastq format were firstly
498 processed through in-house perl scripts. In this step, clean data (clean reads) were obtained
499 by removing reads containing adapter, reads containing ploy-N and low-quality reads from raw
500 data. All the downstream analyses were based on the clean data with high quality. Index of the
501 TAIR10 reference genome was built using Hisat2 v2.0.5 and paired-end clean reads were
502 aligned to the reference genome using Hisat2 v2.0.5. We selected Hisat2 as the mapping tool
503 for that Hisat2 can generate a database of splice junctions based on the gene model
504 annotation file and thus a better mapping result than other non-splice mapping tools.
505 Differential expression analysis was performed using the DESeq2 R package (1.20.0). The
506 resulting p-values were adjusted using the Benjamini and Hochberg's approach for controlling
507 the false discovery rate. Genes with an adjusted p-value <=0.05 found by DESeq2 and a fold
508 change > 2 were assigned as differentially expressed.
509
510 Camalexin quantification
511 To analyze camalexin content in seedlings grown in liquid culture, whole seedlings were
512 freeze-dried at -10°C, -0.370 mbar for 17 hours using the CHRIST ALPHA 2-4 system (Martin
513 Christ, Osterode am Harz, Germany) and their dry weight recorded. For *Colletotrichum*
514 *higginsianum*-infected leaf material, camalexin was directly extracted from sampled leaf discs
515 as described (Nawrath and Métraux, 1999; Engelsdorf et al., 2013). Crude phytochemicals
516 were extracted from the samples in 600 µl 70% methanol supplemented with 50ng ortho-anisic
517 acid (oANI) as internal standard at 65°C for 1 hr. Crude extraction was repeated on the same
518 samples with 90% methanol at 65°C for 1 hour. The two extractions were combined, and a

519 rotatory vacuum concentrator (RVC 2-25 CDplus, Martin Christ) was used to evaporate
520 methanol. Proteins and other biomolecules were precipitated from the extract with 500 µl of 5
521 % trichloroacetic acid. After centrifugation, the supernatant was collected into a fresh reaction
522 tube and partitioned twice against 600 µl of cyclohexane/ethyl acetate (1:1 (v/v)) solution with
523 vigorous shaking and centrifugation at 3,500*g* for 10 min. The combined organic (upper)
524 phases were evaporated in the vacuum concentrator and resuspended in 80% 25 mM
525 potassium dihydrogen phosphate buffer (80%, 25 mM KH_2PO_4, pH 2.6) / 20% acetonitrile
526 (ACN). Camalexin content in the extract was separated on an InfinityLab Poroshell 120 EC-
527 C18 (3.0 x 150 mm 2.7-Micron, Agilent Technologies) column and analyzed using an UHPLC
528 system (1260 Infinity II, Agilent Technologies, Santa Clara, California, USA). The separation
529 was achieved using gradient elution of a mobile phase consisting of (A) 25 mM KH_2PO_4, pH
530 2.6, and (B) 99% ACN at a flow rate of 1 ml/min: 0 – 2.5 min: 20% B; 2.5 – 6 min: 20% to 80%
531 B; 6 – 7 min: 80% B; 7 – 8 min: 80% to 20% B; 8–10 min: 20% B. A 1260 FLD Spectra G712B
532 (Agilent Technologies) fluorescence detector was used to detect oANI (excitation 305 nm,
533 emission 365 nm) and camalexin (excitation 305 nm, emission 370 nm). A standard dilution
534 series of oANI and camalexin in the range of 0.02 to 100 ng employed for quantification.
535 OpenLAb CDS ChemStation software C01.10 (Agilent Technologies) was used to operate the
536 HPLC system and also for quantifying the metabolites.
537
538 <u>MAP kinase phosphorylation assay</u>
539 Ten-day-old seedlings were grown in half-strength Murashige and Skoog (MS) liquid medium
540 [Murashige and Skoog Basal Medium (2.1 g/L), MES (0.5 g/L), and 1% sucrose, pH 5.7] in 12-
541 well plates. Seedlings were subjected to the following treatments in fresh liquid medium at the
542 indicated final concentrations. On the ninth day, the medium was replaced with fresh medium,
543 and on the following day seedlings were treated with either Mock (DMSO), 600 nM ISX, 10 nM
544 AtPep3, or a combined treatment of 600 nM ISX + 10 nM AtPep3 for 10 min, 4 h, or 6 h. Protein
545 extraction was performed as described in Gigli-Bisceglia et al. (2022). For protein extraction,
546 the following buffer was used: 50 mM Tris-HCl (pH 7.5), 200 mM NaCl, 1 mM EDTA, 10% (v/v)
547 glycerol, 0.1% (v/v) Tween 20, 1 mM PMSF, 1 mM DTT, 1× protease inhibitor cocktail (Sigma-
548 Aldrich, P9599), and 1× phosphatase inhibitor cocktail (Sigma-Aldrich, P2850). Samples were
549 incubated on ice for 15 min and centrifuged at 13,000 g for 15 min at 4°C. The resulting
550 supernatants were used for western blot analysis. Protein concentration was determined using
551 the Bradford assay (Bio-Rad). Samples were mixed with 4× loading buffer [240 mM Tris-HCl
552 (pH 6.8), 8% (w/v) SDS, 40% glycerol, 5% β-mercaptoethanol, 0.04% (w/v) Bromophenol Blue]
553 and heated at 95°C for 2 min. Protein samples (35 µg total protein per lane) were separated
554 on 10% SDS-PAGE gels and transferred to nitrocellulose membranes using the Trans-Blot
555 Turbo Transfer System (Bio-Rad) at 25 V, 1.3 A for 7 min. Membranes were blocked in Tris-

556 buffered saline with 0.1% Tween 20 (TBST) containing 5% (w/v) bovine serum albumin (BSA;
557 Sigma-Aldrich, A3608) for 1 h, then incubated overnight with the primary phospho-p44/42
558 MAPK (Erk1/2) (Thr202/Tyr204) antibody (1:2000, Cell Signaling Technology, 9101). After
559 three washes with TBST, membranes were incubated with the secondary HRP-linked anti-
560 rabbit IgG antibody (1:6000, Cell Signaling Technology, 7074) for 2 h. Following three
561 additional washes with TBST, chemiluminescence was detected using Clarity Western ECL
562 Substrate (Bio-Rad, 1705061) for 2 min and visualized with the ChemiDoc imaging system
563 (Bio-Rad). For equal loading analysis, membranes were stripped using stripping solution (100
564 mM Tris-HCl, pH 6.8, 2% SDS, 100 mM β-mercaptoethanol) for 1 h, re-blocked as described
565 above, and probed with the β-Actin (C4) antibody (1:2000, Santa Cruz Biotechnology, sc-
566 47778) for 1 h. Chemiluminescence detection was performed as described previously.
567
568 <u>Ca^{2+} assays</u>
569 To monitor cytosolic Ca^{2+} transients, we employed Arabidopsis reporter lines expressing
570 cytosolic-targeted aequorin in Col-0 (pMAQ2; Knight et al., 1991) and *pec1-1 pec2-1*
571 background (unpublished). The measurements were carried out as described before by
572 Tanaka et al. (2013), with minor alterations to the CTZ buffer. Briefly, seedlings (5 days old)
573 grown sterilely on half-strength Murashige and Skoog (½ MS) medium were transferred into
574 white 96-well plates, each well containing 50 µL of CTZ buffer (1.4 mM $CaCl_2$, 20 mM KCl,
575 5 mM MES-KOH, pH 5.7) supplemented with 10 µM coelenterazine (Cayman Chemical, Ann
576 Arbor, USA). For aequorin reconstitution, seedlings were kept in the dark at 22 °C overnight.
577 For priming experiments, ISX was added at a final concentration of 600 nM 4.5 hours prior to
578 the measurement. Cytosolic Ca^{2+} transients were elicited with 200 mM NaCl. Luminescence
579 was recorded using a TECAN Spark plate reader (Tecan, Männedorf, Switzerland), with an
580 integration time of 500 ms. To determine total aequorin content, seedlings were discharged
581 using 10% ethanol (v/v) and 1 M $CaCl_2$. Calcium levels were calculated from luminescence
582 signals as described by (Knight et al., 1996).
583
584 <u>Confocal microscopy</u>
585 5-day old Arabidopsis seedlings grown on solid ½ MS, 1% Sucrose, 0.8% Agar, pH 5.8 plates,
586 using a light regime of 16-hour photoperiod were incubated in ½ MS pH 5.8 liquid solutions
587 containing 600 nM isoxaben, 10 nM Pep3, a combination of both or corresponding mock
588 controls for the indicated durations. Seedlings were mounted in the same solution they were
589 treated in and imaged using a Leica SP8 confocal microscope equipped with a HC PL 10x/0.3
590 objective, a white light laser and HyD detectors. GFP was excited using 488 nm wavelength
591 and fluorescence emission was detected between 495 nm and 535 nm. Acquisition parameters

were kept constant during experiments. Fluorescence intensity was measured using Fiji (Schindelin et al., 2012).

Variable angle-total internal reflection microscopy (VA-TIRFM)

5-day old Arabidopsis seedlings were grown and treated as described for confocal microscopy. Seedlings were mounted in the same solution they were treated in between two coverslips and imaged using a custom-build microscope platform for variable angle total internal reflection microscopy (VA-TIRFM) (Rohr et al., 2024), equipped with an 100x objective NA 1.49 (Zeiss, 421190-9800-000), a polychromatic modulator (AOTF, AA OPTO-ELECTRONIC) and a sCMOS camera (Hamamatsu Photonics, ORCA-Flash4.0 V2). To ensure that the target laser power value always corresponds to the actual irradiance in the sample plane, the power of each laser line was calibrated before each experiment using a PM100D detector (Thorlabs) as previously described (von Arx et al., 2024). Samples were excited with 488 nm diode laser at 200 µW and 20 seconds stream acquisitions were recorded at 5 Hz for each cell. Acquisition parameters were kept constant during experiments.

Enhanced-super resolution radial fluctuation analyses (eSRRF)

Super-resolved image reconstructions of THE1-GFP plasma membrane organization were computed using eSRRF (Laine et al., 2023) in Fiji (Schindelin et al., 2012). Stream VA-TIRFM acquisitions were processed using the following parameters that were defined by iterative parameter sweep (Laine et al., 2023): magnification = 6, radius = 3, sensitivity = 3 and frames = 100. The average (AVG) reconstructions of THE1-GFP plasma membrane organization were segmented and analysed using Nanonet, an automated custom-made analysis pipeline (https://github.com/NanoSignalingLab/NanoNet), providing nanodomain density and image wide spatial clustering index (iSCI) based on predicted localization density.

Statistical analysis

All statistical analysis were performed with GraphPad Prism (Version 10.5.0). Specific information on statistical methods, sample size, significance level and p-values is provided in the respective figure legends.

Acknowledgements

This work was funded by the Deutsche Forschungsgemeinschaft (DFG, German Research Foundation) grants EN 1071/3-1 (to TE), A08-SFB1101 (to JG) and B01-TRR356 (to JG). H-HK and SM were supported by DFG SFB-TR 175, project B09 (INST 86/2119-2). NGB was supported by the Dutch Research Council (NWO), grant number OCENW.M.24.079.

We are grateful to Debora Gasperini (IPB Halle) for providing *aos* seeds; Stefan Weinl and Jörg Kudla (Universität Münster) for *cas-1* seeds; Erich Glawischnig (TU Munich) for *cyp71a12/a13* seeds; and Kay Schneitz (TU Munich) for *pTHE1::THE1-GFP* seeds. Live cell imaging was performed at the ZMBP microscopy facility of the University of Tübingen and at the Center for Advanced Light Microscopy (CALM) of the TUM School of Life Sciences. We thank Michelle von Arx (TU Munich) for providing access to the NanoNet software prior publication and acknowledge Christiane Rohrbach and Nadja Braun (both Philipps-Universität Marburg) for excellent technical assistance.

Author contributions

Conceptualization and project administration: TE; Investigation: RNM, LF, JD, DB, SM, AR, NGB, TE; Funding acquisition: H-HK, JG, NGB, TE; Supervision: RNM, H-HK, JG, NGB, TE; Writing – original draft: TE; Writing – review & editing: RNM, LF, JD, DB, SM, AR, H-HK, JG, NGB, TE.

Declaration of interests

The authors declare no competing interests.

References

Ahuja I, Kissen R, Bones AM (2012) Phytoalexins in defense against pathogens. Trends in Plant Science **17:** 73-90

Bacete L, Mélida H, Miedes E, Molina A (2018) Plant cell wall-mediated immunity: Cell wall changes trigger disease resistance responses. The Plant Journal **93:** 614-636

Bacete L, Schulz J, Engelsdorf T, Bartosova Z, Vaahtera L, Yan G, Gerhold JM, Tichá T, Øvstebø C, Gigli-Bisceglia N, Johannessen-Starheim S, Margueritat J, Kollist H, Dehoux T, McAdam SAM, Hamann T (2022) THESEUS1 modulates cell wall stiffness and abscisic acid production in *Arabidopsis thaliana*. Proceedings of the National Academy of Sciences **119:** e2119258119

Bartels S, Boller T (2015) Quo vadis, Pep? Plant elicitor peptides at the crossroads of immunity, stress, and development. Journal of Experimental Botany **66:** 5183-5193

Bartels S, Lori M, Mbengue M, van Verk M, Klauser D, Hander T, Böni R, Robatzek S, Boller T (2013) The family of Peps and their precursors in Arabidopsis: differential expression and localization but similar induction of pattern-triggered immune responses. Journal of Experimental Botany **64:** 5309-5321

Birkenbihl RP, Diezel C, Somssich IE (2012) Arabidopsis WRKY33 Is a Key Transcriptional Regulator of Hormonal and Metabolic Responses toward Botrytis cinerea Infection Plant Physiology **159:** 266-285

Birkenbihl RP, Kracher B, Roccaro M, Somssich IE (2017) Induced Genome-Wide Binding of Three Arabidopsis WRKY Transcription Factors during Early MAMP-Triggered Immunity. The Plant Cell **29:** 20-38

Bücherl CA, Jarsch IK, Schudoma C, Segonzac C, Mbengue M, Robatzek S, MacLean D, Ott T, Zipfel C (2017) Plant immune and growth receptors share common signalling components but localise to distinct plasma membrane nanodomains. eLife **6:** e25114

Chaudhary A, Chen X, Gao J, Leśniewska B, Hammerl R, Dawid C, Schneitz K (2020) The Arabidopsis receptor kinase STRUBBELIG regulates the response to cellulose deficiency. PLOS Genetics **16:** e1008433

Chaudhary A, Chen X, Leśniewska B, Boikine R, Gao J, Wolf S, Schneitz K (2021) Cell wall damage attenuates root hair patterning and tissue morphogenesis mediated by the receptor kinase STRUBBELIG. Development **148**

Denness L, McKenna JF, Segonzac C, Wormit A, Madhou P, Bennett M, Mansfield J, Zipfel C, Hamann T (2011) Cell wall damage-induced lignin biosynthesis is regulated by a reactive oxygen species- and jasmonic acid-dependent process in Arabidopsis. Plant Physiology **156:** 1364-1374

Engelsdorf T, Gigli-Bisceglia N, Veerabagu M, McKenna JF, Vaahtera L, Augstein F, Van der Does D, Zipfel C, Hamann T (2018) The plant cell wall integrity maintenance and immune signaling systems cooperate to control stress responses in *Arabidopsis thaliana*. Science Signaling **11**

Engelsdorf T, Horst RJ, Pröls R, Pröschel M, Dietz F, Hückelhoven R, Voll LM (2013) Reduced carbohydrate availability enhances the susceptibility of Arabidopsis toward *Colletotrichum higginsianum*. Plant Physiology **162:** 225-238

Engelsdorf T, Kjaer L, Gigli-Bisceglia N, Vaahtera L, Bauer S, Miedes E, Wormit A, James L, Chairam I, Molina A, Hamann T (2019) Functional characterization of genes mediating cell wall metabolism and responses to plant cell wall integrity impairment. BMC Plant Biology **19:** 320

Engelsdorf T, Will C, Hofmann J, Schmitt C, Merritt BB, Rieger L, Frenger MS, Marschall A, Franke RB, Pattathil S, Voll LM (2017) Cell wall composition and penetration resistance against the fungal pathogen *Colletotrichum higginsianum* are affected by impaired starch turnover in Arabidopsis mutants. Journal of Experimental Botany **68:** 701-713

Feng W, Kita D, Peaucelle A, Cartwright HN, Doan V, Duan Q, Liu M-C, Maman J, Steinhorst L, Schmitz-Thom I, Yvon R, Kudla J, Wu H-M, Cheung AY, Dinneny JR (2018) The FERONIA receptor kinase maintains cell-wall integrity during salt stress through Ca^{2+} signaling. Current Biology **28:** 666-675.e665

Franck CM, Westermann J, Boisson-Dernier A (2018) Plant malectin-like receptor kinases: From cell wall integrity to immunity and beyond. Annual Review of Plant Biology **69:** 301-328

Frerigmann H, Glawischnig E, Gigolashvili T (2015) The role of MYB34, MYB51 and MYB122 in the regulation of camalexin biosynthesis in Arabidopsis thaliana. Frontiers in Plant Science **6:** 654

Gigli Bisceglia N, Savatin DV, Cervone F, Engelsdorf T, De Lorenzo G (2018) Loss of the Arabidopsis Protein Kinases ANPs Affects Root Cell Wall Composition, and Triggers the Cell Wall Damage Syndrome. Frontiers in Plant Science **8**

Gigli-Bisceglia N, Engelsdorf T, Strnad M, Vaahtera L, Khan GA, Yamoune A, Alipanah L, Novák O, Persson S, Hejatko J, Hamann T (2018) Cell wall integrity modulates *Arabidopsis thaliana* cell cycle gene expression in a cytokinin- and nitrate reductase-dependent manner. Development **145:** dev166678

Gigli-Bisceglia N, van Zelm E, Huo W, Lamers J, Testerink C (2022) Arabidopsis root responses to salinity depend on pectin modification and cell wall sensing. Development **149:** dev200363

Glawischnig E (2007) Camalexin. Phytochemistry **68:** 401-406

Gonneau M, Desprez T, Martin M, Doblas VG, Bacete L, Miart F, Sormani R, Hématy K, Renou J, Landrein B, Murphy E, Van De Cotte B, Vernhettes S, De Smet I, Höfte H (2018) Receptor kinase THESEUS1 is a rapid alkalinization factor 34 receptor in Arabidopsis. Current Biology **28:** 2452-2458.e2454

Gronnier J, Franck CM, Stegmann M, DeFalco TA, Abarca A, von Arx M, Dünser K, Lin W, Yang Z, Kleine-Vehn J, Ringli C, Zipfel C (2022) Regulation of immune receptor kinase plasma membrane nanoscale organization by a plant peptide hormone and its receptors. eLife **11:** e74162

Hamann T, Bennett M, Mansfield J, Somerville C (2009) Identification of cell-wall stress as a hexose-dependent and osmosensitive regulator of plant responses. The Plant Journal **57:** 1015-1026

Hander T, Fernández-Fernández ÁD, Kumpf RP, Willems P, Schatowitz H, Rombaut D, Staes A, Nolf J, Pottie R, Yao P, Gonçalves A, Pavie B, Boller T, Gevaert K, Van Breusegem F, Bartels S, Stael S (2019) Damage on plants activates Ca2+-dependent metacaspases for release of immunomodulatory peptides. Science **363:** eaar7486

Hdedeh O, Mercier C, Poitout A, Martinière A, Zelazny E (2025) Membrane nanodomains to shape plant cellular functions and signaling. New Phytologist **245:** 1369-1385

He Y, Xu J, Wang X, He X, Wang Y, Zhou J, Zhang S, Meng X (2019) The Arabidopsis Pleiotropic Drug Resistance Transporters PEN3 and PDR12 Mediate Camalexin Secretion for Resistance to Botrytis cinerea. The Plant Cell **31:** 2206-2222

Hématy K, Sado P-E, Van Tuinen A, Rochange S, Desnos T, Balzergue S, Pelletier S, Renou J-P, Höfte H (2007) A receptor-like kinase mediates the response of Arabidopsis cells to the inhibition of cellulose synthesis. Current Biology **17:** 922-931

Hou S, Liu D, Huang S, Luo D, Liu Z, Xiang Q, Wang P, Mu R, Han Z, Chen S, Chai J, Shan L, He P (2021) The Arabidopsis MIK2 receptor elicits immunity by sensing a conserved signature from phytocytokines and microbes. Nature Communications **12:** 5494

Jaillais Y, Bayer E, Bergmann DC, Botella MA, Boutté Y, Bozkurt TO, Caillaud M-C, Germain V, Grossmann G, Heilmann I, Hemsley PA, Kirchhelle C, Martinière A, Miao Y, Mongrand S, Müller S, Noack LC, Oda Y, Ott T, Pan X, Pleskot R, Potocky M, Robert S, Rodriguez CS, Simon-Plas F, Russinova E, Van Damme D, Van Norman JM, Weijers D, Yalovsky S, Yang Z, Zelazny E, Gronnier J (2024) Guidelines for naming and studying plasma membrane domains in plants. Nature Plants **10:** 1172-1183

Jolivet M-D, Deroubaix AF, Boudsocq M, Abel NB, Rocher M, Robbe T, Wattelet-Boyer V, Huard J, Lefebvre D, Lu Y-J, Day B, Saias G, Ahmed J, Cotelle V, Giovinazzo N, Gallois J-L, Yamaji Y, German-Retana S, Gronnier J, Ott T, Mongrand S, Germain V (2025) Interdependence of plasma membrane nanoscale dynamics of a kinase and its cognate substrate underlies Arabidopsis response to viral infection. eLife **12:** RP90309

Knight H, Trewavas AJ, Knight MR (1996) Cold calcium signaling in Arabidopsis involves two cellular pools and a change in calcium signature after acclimation. The Plant Cell **8:** 489-503

Knight MR, Campbell AK, Smith SM, Trewavas AJ (1991) Transgenic plant aequorin reports the effects of touch and cold-shock and elicitors on cytoplasmic calcium. Nature **352:** 524-526

Konopka CA, Bednarek SY (2008) Variable-angle epifluorescence microscopy: a new way to look at protein dynamics in the plant cell cortex. The Plant Journal **53:** 186-196

Laine RF, Heil HS, Coelho S, Nixon-Abell J, Jimenez A, Wiesner T, Martínez D, Galgani T, Régnier L, Stubb A, Follain G, Webster S, Goyette J, Dauphin A, Salles A, Culley S, Jacquemet G, Hajj B, Leterrier C, Henriques R (2023) High-fidelity 3D live-cell nanoscopy through data-driven enhanced super-resolution radial fluctuation. Nature Methods **20:** 1949-1956

Li Y, Liu K, Tong G, Xi C, Liu J, Zhao H, Wang Y, Ren D, Han S (2021) MPK3/MPK6-mediated phosphorylation of ERF72 positively regulates resistance to Botrytis cinerea through directly and indirectly activating the transcription of camalexin biosynthesis enzymes. Journal of Experimental Botany **73:** 413-428

Liu M-CJ, Yeh F-LJ, Yvon R, Simpson K, Jordan S, Chambers J, Wu H-M, Cheung AY (2024) Extracellular pectin-RALF phase separation mediates FERONIA global signaling function. Cell **187:** 312-330.e322

Mao G, Meng X, Liu Y, Zheng Z, Chen Z, Zhang S (2011) Phosphorylation of a WRKY Transcription Factor by Two Pathogen-Responsive MAPKs Drives Phytoalexin Biosynthesis in Arabidopsis. The Plant Cell **23:** 1639-1653

Marquis V, Smirnova E, Graindorge S, Delcros P, Villette C, Zumsteg J, Heintz D, Heitz T (2022) Broad-spectrum stress tolerance conferred by suppressing jasmonate signaling attenuation in Arabidopsis JASMONIC ACID OXIDASE mutants. The Plant Journal **109:** 856-872

Martinière A, Lavagi I, Nageswaran G, Rolfe DJ, Maneta-Peyret L, Luu D-T, Botchway SW, Webb SED, Mongrand S, Maurel C, Martin-Fernandez ML, Kleine-Vehn J, Friml J, Moreau P, Runions J (2012) Cell wall constrains lateral diffusion of plant plasma-membrane proteins. Proceedings of the National Academy of Sciences **109:** 12805-12810

McKenna JF, Rolfe DJ, Webb SED, Tolmie AF, Botchway SW, Martin-Fernandez ML, Hawes C, Runions J (2019) The cell wall regulates dynamics and size of plasma-membrane nanodomains in Arabidopsis. Proceedings of the National Academy of Sciences **116:** 12857-12862

Merz D, Richter J, Gonneau M, Sanchez-Rodriguez C, Eder T, Sormani R, Martin M, Hématy K, Höfte H, Hauser M-T (2017) T-DNA alleles of the receptor kinase THESEUS1 with opposing effects on cell wall integrity signaling. Journal of Experimental Botany **68:** 4583-4593

Mielke S, Zimmer M, Meena MK, Dreos R, Stellmach H, Hause B, Voiniciuc C, Gasperini D (2021) Jasmonate biosynthesis arising from altered cell walls is prompted by turgor-driven mechanical compression. Science Advances **7:** eabf0356

Millard PS, Weber K, Kragelund BB, Burow M (2019) Specificity of MYB interactions relies on motifs in ordered and disordered contexts. Nucleic Acids Research **47:** 9592-9608

Molina A, Miedes E, Bacete L, Rodríguez T, Mélida H, Denancé N, Sánchez-Vallet A, Rivière M-P, López G, Freydier A, Barlet X, Pattathil S, Hahn M, Goffner D (2021) Arabidopsis cell wall composition determines disease resistance specificity and fitness. Proceedings of the National Academy of Sciences **118:** e2010243118

Monsalvo I, Parasecolo L, Pullano S, Lin J, Shahabi A, Ly M, Kwon H, Mathur K, Rodrillo KAM, Ifa DR, Kovinich N (2025) ANAC042 Regulates the Biosynthesis of Conserved- and Lineage-Specific Phytoalexins in Arabidopsis. International Journal of Molecular Sciences **26:** 3683

Mucha S, Heinzlmeir S, Kriechbaumer V, Strickland B, Kirchhelle C, Choudhary M, Kowalski N, Eichmann R, Hückelhoven R, Grill E, Kuster B, Glawischnig E (2019) The Formation of a Camalexin Biosynthetic Metabolon. The Plant Cell **31:** 2697-2710

Müller TM, Böttcher C, Morbitzer R, Götz CC, Lehmann J, Lahaye T, Glawischnig E (2015) TRANSCRIPTION ACTIVATOR-LIKE EFFECTOR NUCLEASE-Mediated Generation and Metabolic Analysis of Camalexin-Deficient *cyp71a12 cyp71a13* Double Knockout Lines. Plant Physiology **168:** 849-858

Munzert KS, Engelsdorf T (2025) Plant cell wall structure and dynamics in plant–pathogen interactions and pathogen defence. Journal of Experimental Botany **76:** 228-242

Nakagawa Y, Katagiri T, Shinozaki K, Qi Z, Tatsumi H, Furuichi T, Kishigami A, Sokabe M, Kojima I, Sato S, Kato T, Tabata S, Iida K, Terashima A, Nakano M, Ikeda M, Yamanaka T, Iida H (2007) Arabidopsis plasma membrane protein crucial for Ca2+ influx and touch sensing in roots. Proceedings of the National Academy of Sciences **104:** 3639-3644

Nakaminami K, Okamoto M, Higuchi-Takeuchi M, Yoshizumi T, Yamaguchi Y, Fukao Y, Shimizu M, Ohashi C, Tanaka M, Matsui M, Shinozaki K, Seki M, Hanada K (2018) AtPep3 is a hormone-like peptide that plays a role in the salinity stress tolerance of plants. Proceedings of the National Academy of Sciences **115:** 5810-5815

Nawrath C, Métraux J-P (1999) Salicylic Acid Induction–Deficient Mutants of Arabidopsis Express PR-2 and PR-5 and Accumulate High Levels of Camalexin after Pathogen Inoculation. The Plant Cell **11:** 1393-1404

Nomura H, Komori T, Kobori M, Nakahira Y, Shiina T (2008) Evidence for chloroplast control of external Ca2+-induced cytosolic Ca2+ transients and stomatal closure. The Plant Journal **53:** 988-998

Nomura H, Komori T, Uemura S, Kanda Y, Shimotani K, Nakai K, Furuichi T, Takebayashi K, Sugimoto T, Sano S, Suwastika IN, Fukusaki E, Yoshioka H, Nakahira Y, Shiina T (2012) Chloroplast-mediated activation of plant immune signalling in Arabidopsis. Nature Communications **3:** 926

Novaković L, Guo T, Bacic A, Sampathkumar A, Johnson KL (2018) Hitting the Wall—Sensing and Signaling Pathways Involved in Plant Cell Wall Remodeling in Response to Abiotic Stress. Plants **7:** 89

O'Connell R, Herbert C, Sreenivasaprasad S, Khatib M, Esquerré-Tugayé M-T, Dumas B (2004) A novel Arabidopsis-*Colletotrichum* pathosystem for the molecular dissection of plant-fungal interactions. Molecular Plant-Microbe Interactions **17:** 272-282

Ortiz-Morea FA, Liu J, Shan L, He P (2022) Malectin-like receptor kinases as protector deities in plant immunity. Nature Plants **8:** 27-37

Paredez AR, Somerville CR, Ehrhardt DW (2006) Visualization of cellulose synthase demonstrates functional association with microtubules. Science **312:** 1491-1495

Pastorczyk M, Kosaka A, Piślewska-Bednarek M, López G, Frerigmann H, Kułak K, Glawischnig E, Molina A, Takano Y, Bednarek P (2020) The role of CYP71A12 monooxygenase in pathogen-triggered tryptophan metabolism and Arabidopsis immunity. New Phytologist **225:** 400-412

Perraki A, Gronnier J, Gouguet P, Boudsocq M, Deroubaix A-F, Simon V, German-Retana S, Legrand A, Habenstein B, Zipfel C, Bayer E, Mongrand S, Germain V (2018) REM1.3's phospho-status defines its plasma membrane nanodomain organization and activity in restricting PVX cell-to-cell movement. PLOS Pathogens **14:** e1007378

Rhodes J, Yang H, Moussu S, Boutrot F, Santiago J, Zipfel C (2021) Perception of a divergent family of phytocytokines by the Arabidopsis receptor kinase MIK2. Nature Communications **12:** 705

Rohr L, Ehinger A, Rausch L, Glöckner Burmeister N, Meixner AJ, Gronnier J, Harter K, Kemmerling B, zur Oven-Krockhaus S (2024) OneFlowTraX: a user-friendly software for super-resolution analysis of single-molecule dynamics and nanoscale organization. Frontiers in Plant Science **15:** 1358935

Saga H, Ogawa T, Kai K, Suzuki H, Ogata Y, Sakurai N, Shibata D, Ohta D (2012) Identification and characterization of ANAC042, a transcription factor family gene involved in the regulation of camalexin biosynthesis in Arabidopsis. Molecular Plant-Microbe Interactions **25:** 684-696

Schindelin J, Arganda-Carreras I, Frise E, Kaynig V, Longair M, Pietzsch T, Preibisch S, Rueden C, Saalfeld S, Schmid B, Tinevez J-Y, White DJ, Hartenstein V, Eliceiri K, Tomancak P, Cardona A (2012) Fiji: an open-source platform for biological-image analysis. Nature Methods **9:** 676-682

Schmidt A, Mächtel R, Ammon A, Engelsdorf T, Schmitz J, Maurino VG, Voll LM (2020) Reactive oxygen species dosage in Arabidopsis chloroplasts can improve resistance towards Colletotrichum higginsianum by the induction of WRKY33. New Phytologist **226:** 189-204

Schoenaers S, Vissenberg K (2025) Overlooked aspects of CrRLK1L–RALF signaling. New Phytologist

Shen W, Liu J, Li J-F (2019) Type-II metacaspases mediate the processing of plant elicitor peptides in Arabidopsis. Molecular Plant **12:** 1524-1533

Tanaka K, Choi J, Stacey G (2013) Aequorin Luminescence-Based Functional Calcium Assay for Heterotrimeric G-Proteins in Arabidopsis. *In* MP Running, ed, G Protein-Coupled Receptor Signaling in Plants: Methods and Protocols. Humana Press, Totowa, NJ, pp 45-54

Tang J, Han Z, Sun Y, Zhang H, Gong X, Chai J (2015) Structural basis for recognition of an endogenous peptide by the plant receptor kinase PEPR1. Cell Research **25:** 110-120

Vaahtera L, Schulz J, Hamann T (2019) Cell wall integrity maintenance during plant development and interaction with the environment. Nature Plants **5:** 924-932

Van der Does D, Boutrot F, Engelsdorf T, Rhodes J, McKenna JF, Vernhettes S, Koevoets I, Tintor N, Veerabagu M, Miedes E, Segonzac C, Roux M, Breda AS, Hardtke CS, Molina A, Rep M, Testerink C, Mouille G, Höfte H, Hamann T, Zipfel C (2017) The Arabidopsis leucine-rich repeat receptor kinase MIK2/LRR-KISS connects cell wall integrity sensing, root growth and response to abiotic and biotic stresses. PLOS Genetics **13:** e1006832

Völkner C, Holzner LJ, Day PM, Ashok AD, Vries Jd, Bölter B, Kunz H-H (2021) Two plastid POLLUX ion channel-like proteins are required for stress-triggered stromal Ca2+release. Plant Physiology **187:** 2110-2125

Voll LM, Zell MB, Engelsdorf T, Saur A, Wheeler MG, Drincovich MF, Weber APM, Maurino VG (2012) Loss of cytosolic NADP-malic enzyme 2 in Arabidopsis thaliana is associated with enhanced susceptibility to *Colletotrichum higginsianum*. New Phytologist **195:** 189-202

von Arx M, Xhelilaj K, Schulz P, zur Oven-Krockhaus S, Gronnier J (2024) Photochromic reversion enables long-term tracking of single molecules in living plants. bioRxiv**:** 2024.2004.2010.585335

Weinl S, Held K, Schlücking K, Steinhorst L, Kuhlgert S, Hippler M, Kudla J (2008) A plastid protein crucial for Ca2+-regulated stomatal responses. New Phytologist **179:** 675-686

Wolf S (2022) Cell Wall Signaling in Plant Development and Defense. Annual Review of Plant Biology **73:** 323-353

Wormit A, Butt SM, Chairam I, McKenna JF, Nunes-Nesi A, Kjaer L, O'Donnelly K, Fernie AR, Woscholski R, Barter MCL, Hamann T (2012) Osmosensitive changes of carbohydrate metabolism in response to cellulose biosynthesis inhibition. Plant Physiology **159:** 105-117

Yamaguchi Y, Huffaker A, Bryan AC, Tax FE, Ryan CA (2010) PEPR2 Is a Second Receptor for the Pep1 and Pep2 Peptides and Contributes to Defense Responses in Arabidopsis The Plant Cell **22:** 508-522

Yamaguchi Y, Pearce G, Ryan CA (2006) The cell surface leucine-rich repeat receptor for *At*Pep1, an endogenous peptide elicitor in Arabidopsis, is functional in transgenic tobacco cells. Proceedings of the National Academy of Sciences **103:** 10104-10109

Zhai K, Rhodes J, Zipfel C (2024) A peptide-receptor module links cell wall integrity sensing to pattern-triggered immunity. Nature Plants **10:** 2027-2037

Zhang C, Wu Y, Liu J, Song B, Yu Z, Li J-F, Yang C, Lai J (2025) SUMOylation controls peptide processing to generate damage-associated molecular patterns in Arabidopsis. Developmental Cell **60:** 696-705.e694

Zhang Z, Gigli-Bisceglia N, Li W, Li S, Wang J, Liu J, Testerink C, Guo Y (2024) SCOOP10 and SCOOP12 peptides act through MIK2 receptor-like kinase to antagonistically regulate Arabidopsis leaf senescence. Molecular Plant **17:** 1805-1819

Zheng Z, Qamar SA, Chen Z, Mengiste T (2006) Arabidopsis WRKY33 transcription factor is required for resistance to necrotrophic fungal pathogens. The Plant Journal **48:** 592-605

Zhou J, Mu Q, Wang X, Zhang J, Yu H, Huang T, He Y, Dai S, Meng X (2022) Multilayered synergistic regulation of phytoalexin biosynthesis by ethylene, jasmonate, and MAPK signaling pathways in Arabidopsis. The Plant Cell **34:** 3066-3087

Zhou J, Wang X, He Y, Sang T, Wang P, Dai S, Zhang S, Meng X (2020) Differential phosphorylation of the transcription factor WRKY33 by the protein kinases CPK5/CPK6 and MPK3/MPK6 cooperatively regulates camalexin biosynthesis in Arabidopsis. The Plant Cell **32:** 2621-2638

Figures

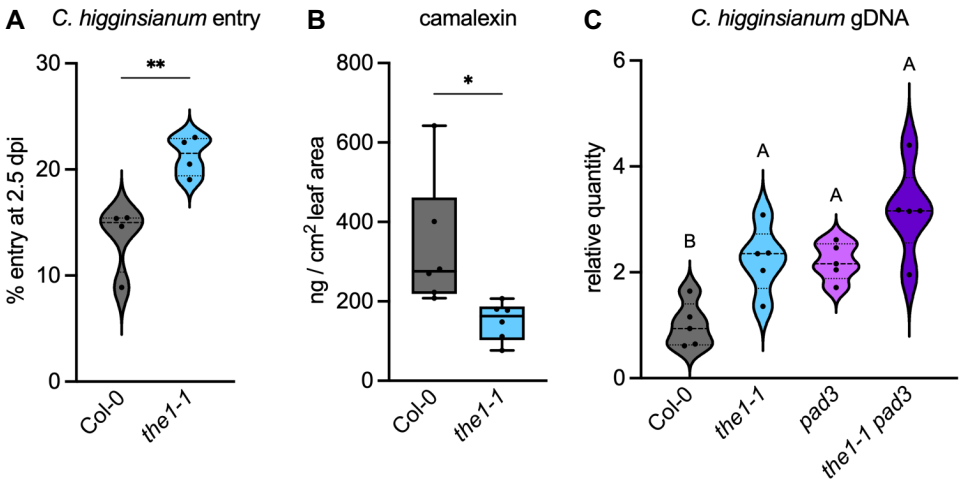

Figure 1: THE1 and camalexin biosynthesis have overlapping roles in resistance to *Colletotrichum higginsianum* infection.
(A) Entry rate of *C. higginsianum* on Col-0 and *the1-1* leaves at 2.5 days post infection (dpi) (n=4). (B) Camalexin amount in infected Col-0 and *the1-1* leaves at 2.5 dpi (n=6). Asterisks in (A,B) indicate statistically significant differences to Col-0 according to a Student's t-test (*$p < 0.05$, **$p < 0.01$). (C) The relative quantity of *C. higginsianum* DNA was determined at 4 dpi in Col-0, *the1-1*, *pad3* and *the1-1 pad3* (n=5). Different letters indicate statistically significant differences according to one-way ANOVA and Holm-Sidak's multiple comparisons test ($\alpha = 0.05$).

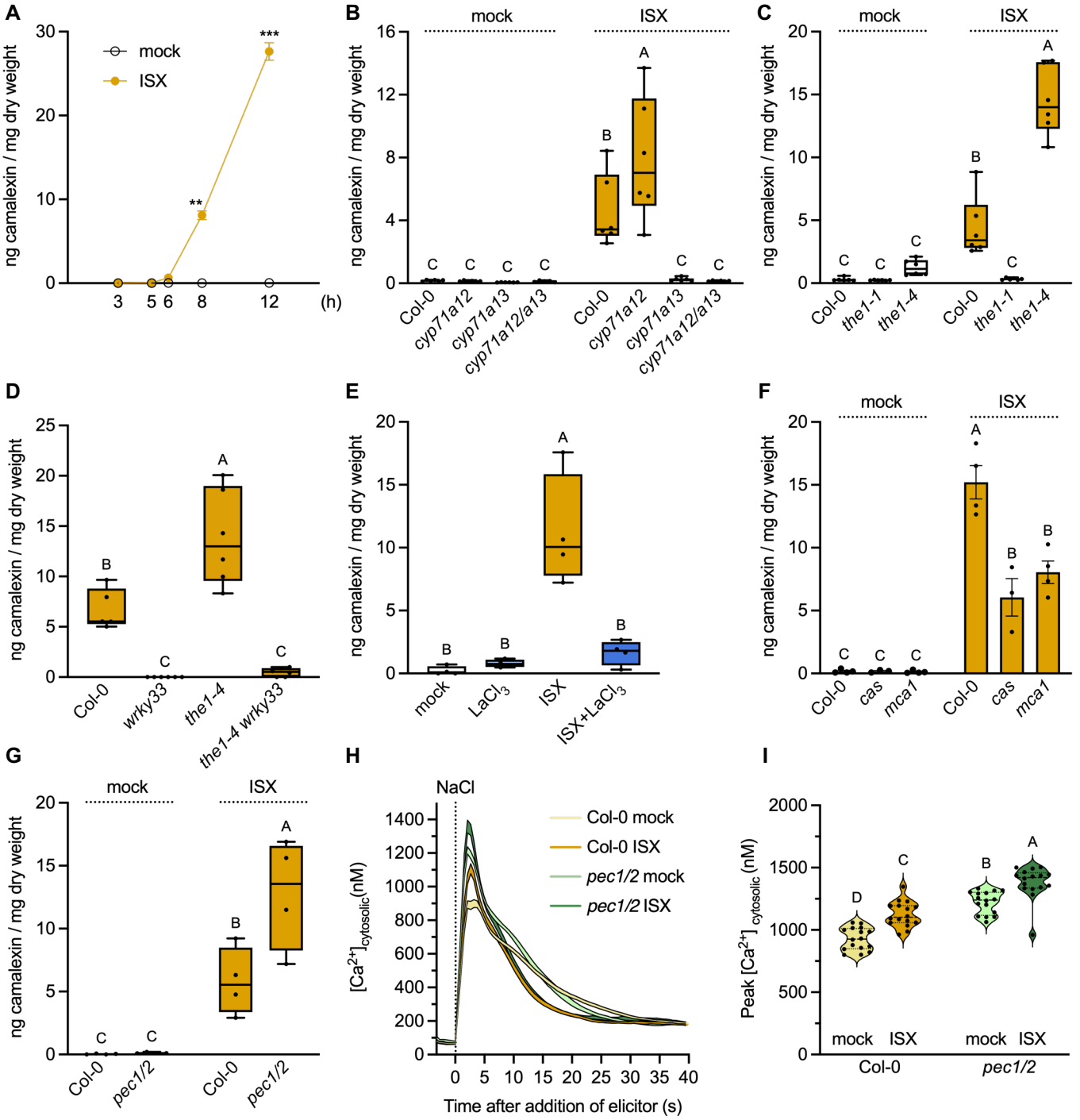

Figure 2: Isoxaben induces camalexin accumulation via THESEUS1, WRKY33 and calcium signaling. (A) Camalexin amount in Col-0 seedlings was determined at 3, 5, 6, 8 and 12 h after mock and isoxaben (ISX) treatment (n=3). Error bars indicate the SEM. Asterisks indicate statistically significant differences between ISX and mock according to a Student's t-test (*p < 0.05, **p < 0.01, ***p < 0.001). (B-G) Camalexin amount in (B) Col-0, *cyp71a12*, *cyp71a13* and *cyp71a12/a13* at 8 h after mock and ISX (n=5-6); (C) Col-0, *the1-1* and *the1-4* at 8 h after mock and ISX (n=6); (D) Col-0, *wrky33*, *the1-4* and *the1-4 wrky33* at 8 h after ISX (n=5-6); (E) Col-0 at 8 h after mock, $LaCl_3$, ISX and ISX+$LaCl_3$ (n=4); (F) Col-0, *cas* and *mca1* at 8 h after mock and ISX (n=3-4; error bars indicate the SEM) and (G) Col-0 and *pec1/2* at 8 h after mock and ISX treatment (n=4). (H) Cytosolic Ca^{2+} concentration in Col-0 and *pec1/2* seedlings after elicitation with 200 mM NaCl. Prior to elicitation, seedlings were treated for 4.5 h with mock or ISX (n=16). The shaded area indicates the SEM. (I) Peak Ca^{2+} values of transients in (H). Different letters indicate statistically significant differences according to (D,E) one-way ANOVA or (B,C,F,H) two-way ANOVA and Holm-Sidak's multiple comparisons test (α = 0.05).

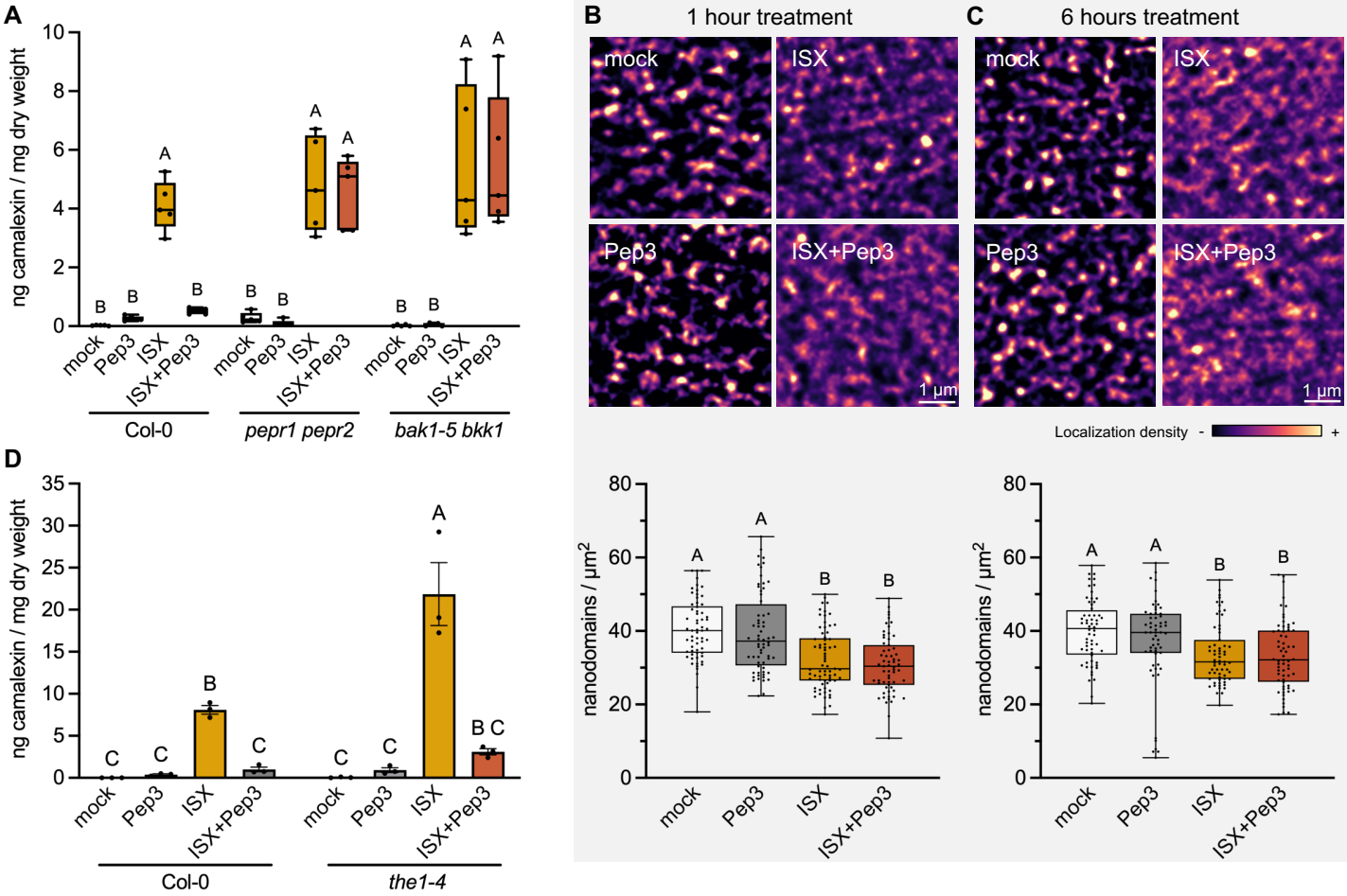

Figure 3: Pep3-PEPR signaling impairs induction of camalexin synthesis downstream of THE1. (A) Camalexin amount in Col-0, *pepr1 pepr2* and *bak1-5 bkk1* seedlings at 8 h after mock, Pep3, isoxaben (ISX) and ISX+Pep3 treatment (n=5). Different letters indicate statistically significant differences according to two-way ANOVA and Holm-Sidak's multiple comparisons test (α = 0.05). (B,C) THE1-GFP nanodomain density was determined in seedling hypocotyls at (B) 1 h and (C) 6 h after treatment with mock, Pep3, ISX and ISX+Pep3. Representative images of enhanced super-resolution radial fluctuation (eSRRF) analysis are shown alongside the quantification of nanodomain density in 3 pooled experiments with 4-8 cells from 3 seedlings per experiment (n=58-69). Different letters indicate statistically significant differences according to Kruskal-Wallis and Dunn's test (α = 0.05). (D) Camalexin amount in Col-0 and *the1-4* seedlings at 8 h after mock, Pep3, ISX and ISX+Pep3 treatment (n=3). Error bars indicate the SEM. Different letters indicate statistically significant differences according to two-way ANOVA and Holm-Sidak's multiple comparisons test (α = 0.05).

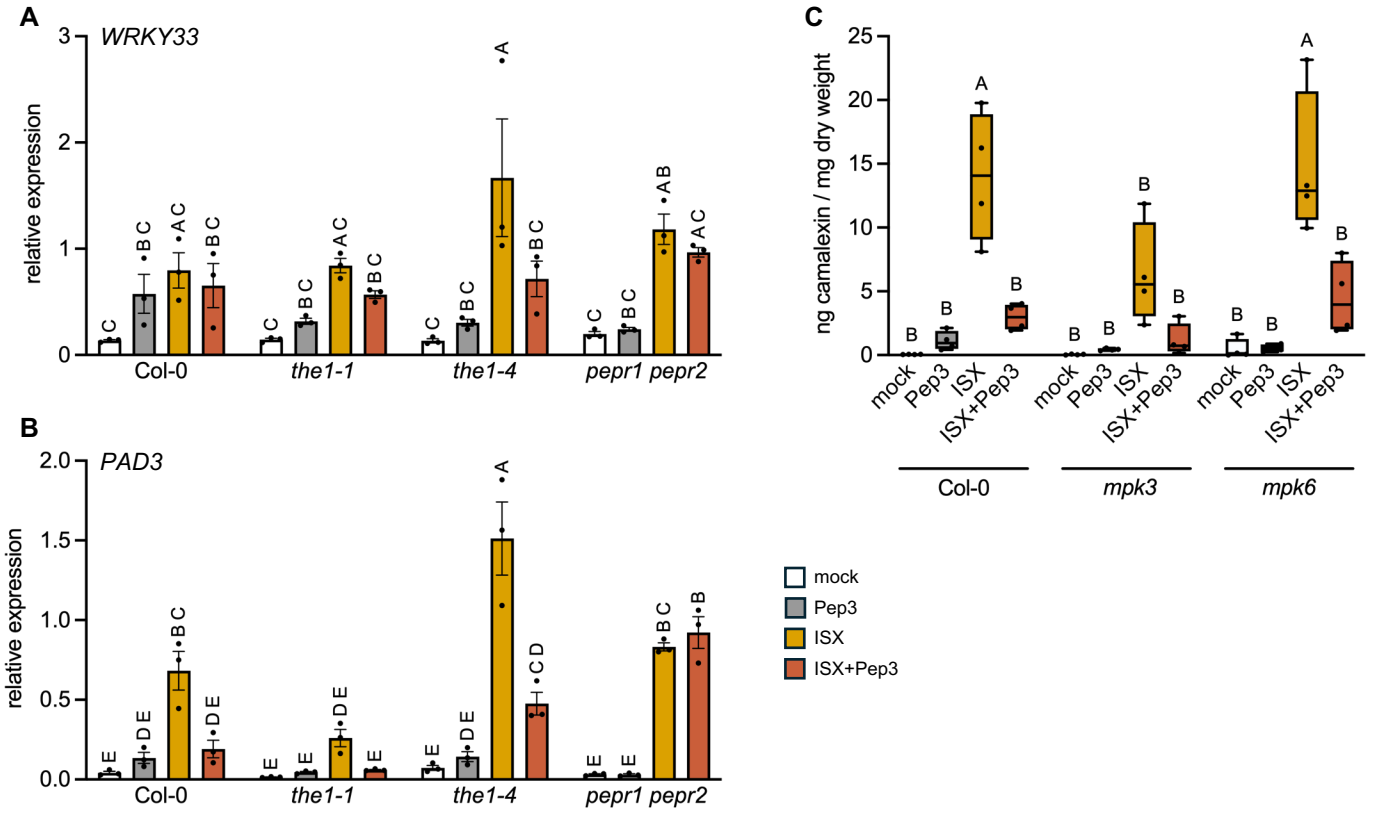

Figure 4: Pep3-dependent inhibition of CWI signaling does not involve WRKY33 and MPK3/6. Relative expression of (A) *WRKY33* and (B) *PAD3* was determined in Col-0, *the1-1*, *the1-4* and *pepr1 pepr2* at 6 h after treatment with mock, Pep3, isoxaben (ISX) and ISX+Pep3 via quantitative RT-PCR. Values are relative to *ACT2* expression and error bars represent the SEM (n=3). (C) Camalexin amount in Col-0, *mpk3* and *mpk6* seedlings at 8 h after mock, Pep3, ISX and ISX+Pep3 treatment (n=4). Different letters indicate statistically significant differences according to two-way ANOVA and Holm-Sidak's multiple comparisons test (α = 0.05).

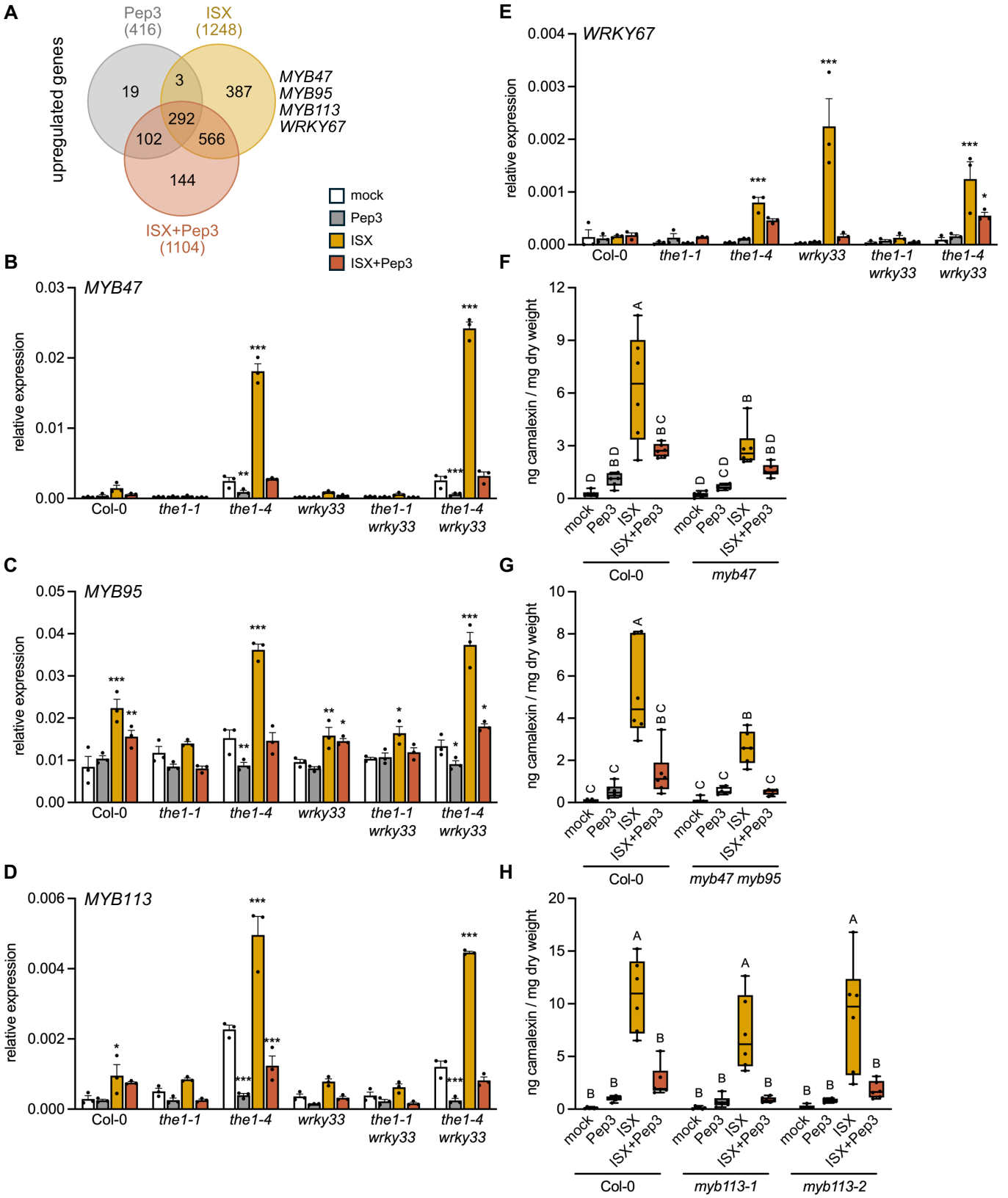

Figure 5: Identification of Pep3-regulated transcription factors involved in ISX-induced camalexin accumulation.

(A) RNA-Sequencing of Col-0 seedlings identifies genes upregulated at 6 h after treatment with mock, Pep3, isoxaben (ISX) and ISX+Pep3 (α = 0.05, fold change >2). (B-E) Relative expression of (B) *MYB47*, (C) *MYB95,* (D) *MYB113* and (E) *WRKY67* was determined in Col-0, *the1-1*, *the1-4, wrky33, the1-1 wrky33* and *the1-4 wrky33* at 6 h after treatment with mock, Pep3, ISX and ISX+Pep3 via quantitative RT-PCR. Values are relative to *ACT2* expression and error bars represent the SEM (n=3). Asterisks indicate statistically significant differences to the respective mock treatments according to two-way ANOVA and Holm-Sidak's multiple comparisons test (*p < 0.05, **p < 0.01, ***p < 0.001). (F-H) Camalexin amount in (F) Col-0 and *myb47*; (G) Col-0 and *myb47 myb95* and (H) Col-0, *myb113-1* and *myb113-2* seedlings at 8 h after mock, Pep3, ISX and ISX+Pep3 treatment (n=6). Different letters indicate statistically significant differences according to two-way ANOVA and Holm-Sidak's multiple comparisons test (α = 0.05).

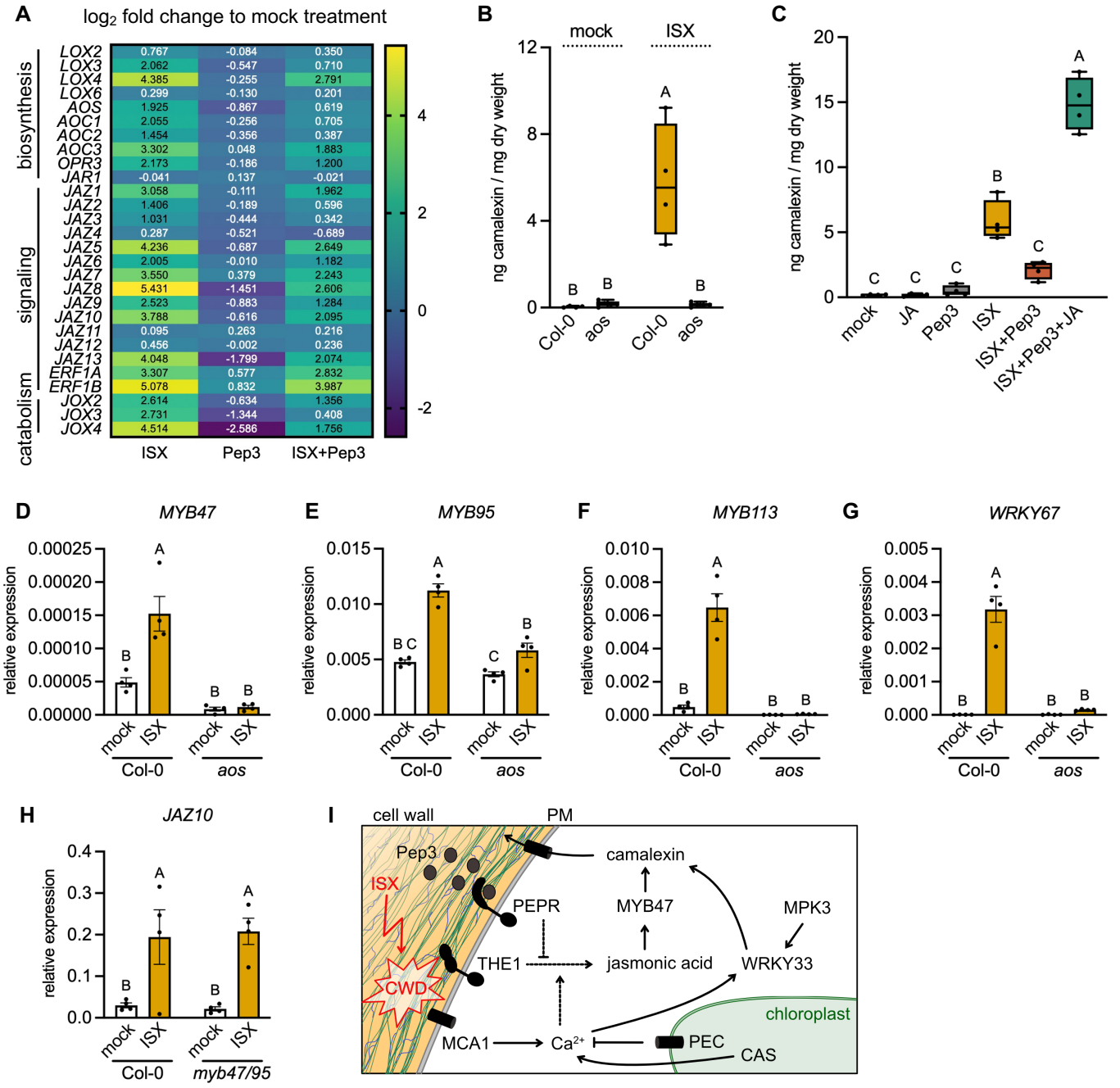

Figure 6: ISX-induced and Pep3-sensitive camalexin accumulation depends on jasmonic acid. (A) Transcripts involved in jasmonic acid (JA) biosynthesis, signaling and catabolism were analyzed via RNA-Sequencing in Col-0 seedlings treated with mock, Pep3, isoxaben (ISX) and ISX+Pep3 for 6 h. Relative expression after ISX, Pep3 and ISX+Pep3 compared to mock treatment is listed as $\log_2$ fold change and visualized as heat map indicating downregulation (dark blue) and upregulation (yellow) of transcripts. (B, C) Camalexin amount in (B) Col-0 and *aos* seedlings at 8 h after mock and ISX treatment (n=4-5) and (C) Col-0 seedlings at 8 h after mock, JA, Pep3, ISX, ISX+Pep3 and ISX+Pep3+JA treatment (n=4). (D-G) Relative expression of (D) *MYB47*, (E) *MYB95,* (F) *MYB113* and (G) *WRKY67* was determined in Col-0 and *aos* seedlings at 6 h after treatment with mock and ISX via quantitative RT-PCR. (H) Relative expression of *JAZ10* was determined in Col-0 and *myb47/95* seedlings at 6 h after treatment with mock and ISX via quantitative RT-PCR. Values in (D-H) are relative to *ACT2* expression and error bars represent the SEM (n=3). Different letters indicate statistically significant differences according to (C) one-way ANOVA or (B, D, E, F, G, H) two-way ANOVA and Holm-Sidak's multiple comparisons test (α = 0.05). (I) Model depicting the induction of camalexin synthesis after perception of cell wall damage (CWD) via THE1 and JA. Interactions with Pep3/PEPR-, WRKY33-, and Ca^{2+} signaling are proposed based on data presented in this manuscript and references discussed in the main text.

Supplemental Figures

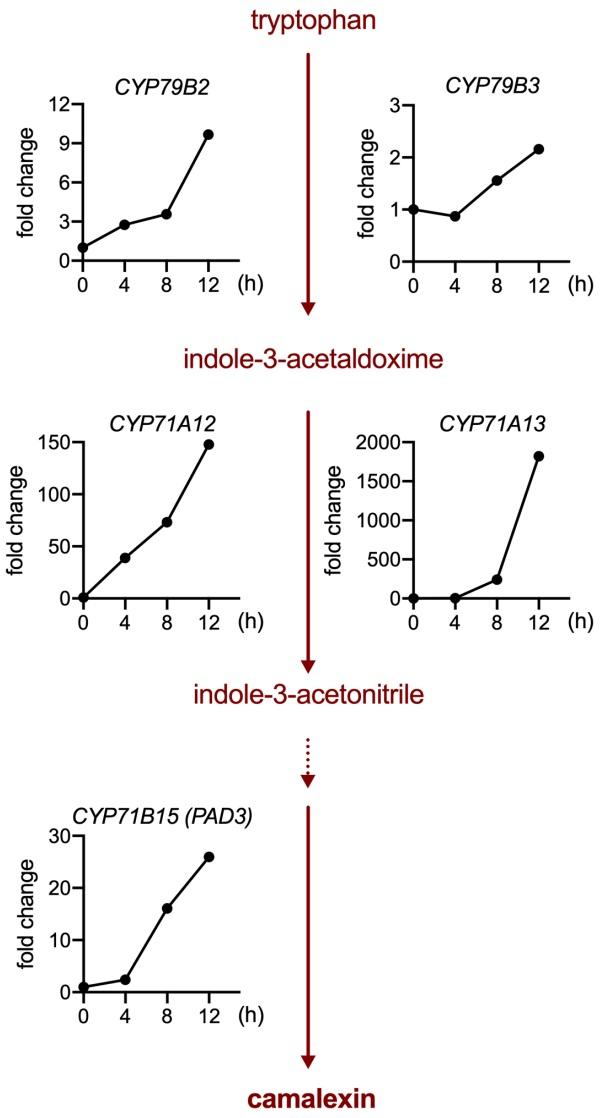

Figure S1: Published transcriptomics data suggest activation of the camalexin biosynthesis pathway by isoxaben treatment.
Relative gene expression of *CYP79B2*, *CAP79B3*, *CYP71A12*, *CYP71A13* and *CYP71B15*/*PAD3* after 0, 4, 8 and 12 h of isoxaben (ISX) treatment compared to t = 0 h (fold change). Microarray data were taken from Hamann et al. (2009). Graphs are positioned along the camalexin biosynthesis pathway according to the enzymatic functions encoded by the genes.

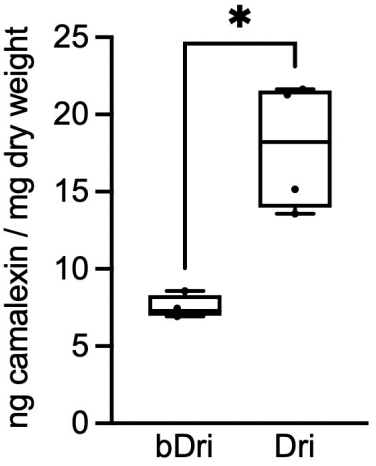

Figure S2: Camalexin accumulates after Driselase treatment.
Camalexin amount in Col-0 seedlings was determined at 8 h after treatment with boiled Driselase (bDri) or Driselase (Dri) (n=4). Asterisks indicate statistically significant differences according to a Student's t-test (*$p < 0.05$).

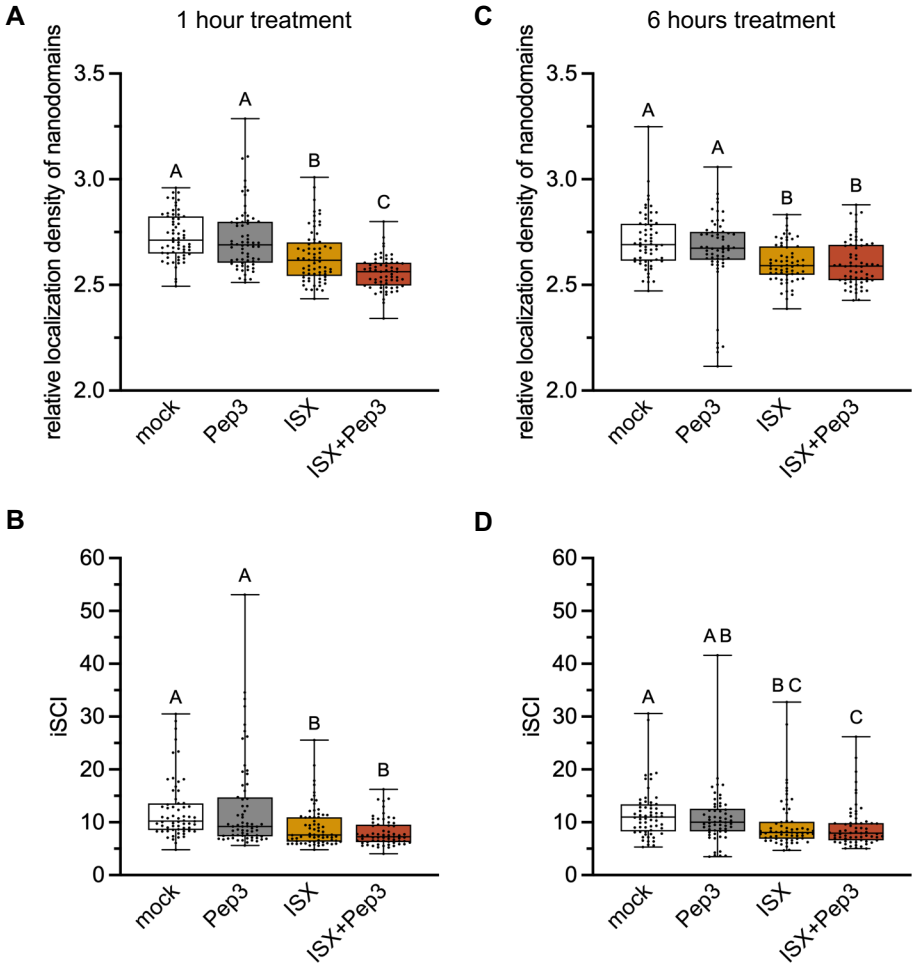

Figure S3: THE1-GFP plasma membrane nanodomain organization after ISX, Pep3 and combined treatments.

THE1-GFP nanodomain organization was analyzed with variable angle total internal reflection microscopy (VA-TIRFM) in combination with enhanced-super resolution radial fluctuation analyses (eSRRF) in seedling hypocotyls at (A, B) 1 h and (C, D) 6 h after treatment with mock, Pep3, isoxaben (ISX) and ISX+Pep3. (A, C) relative localization density of nanodomains and (B, D) mean image wide spatial clustering index (iSCI) per cell were recorded in three pooled experiments with 4-8 cells from three seedlings per experiment (n=58-69). Different letters indicate statistically significant differences according to Kruskal-Wallis and Dunn's test ($\alpha = 0.05$).

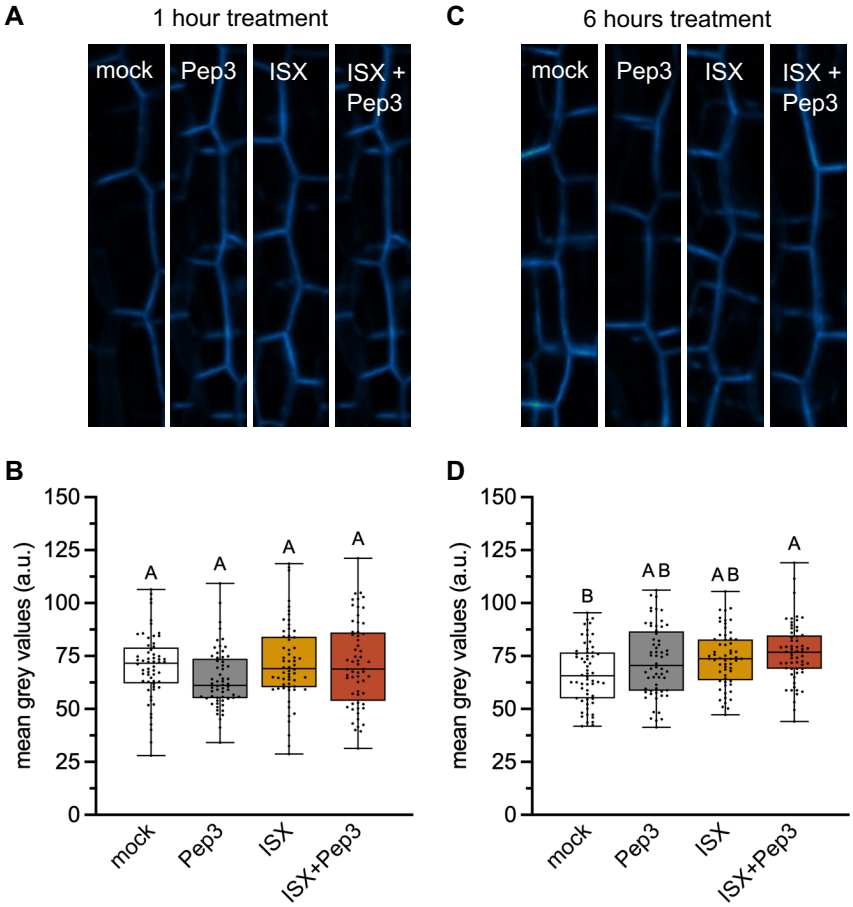

Figure S4: THE1-GFP localization to the plasma membrane after ISX, Pep3 and combined treatments.

THE1-GFP fluorescence intensity was determined in seedling hypocotyls at (A, B) 1 h and (C, D) 6 h after treatment with mock, Pep3, isoxaben (ISX) and ISX+Pep3. (A, C) Representative images taken with confocal laser scanning microscopy. (B, D) Mean grey values recorded in two pooled experiments with 10 cells from three seedlings per experiment (n=60). Different letters indicate statistically significant differences according to Kruskal-Wallis and Dunn's test (α = 0.05).

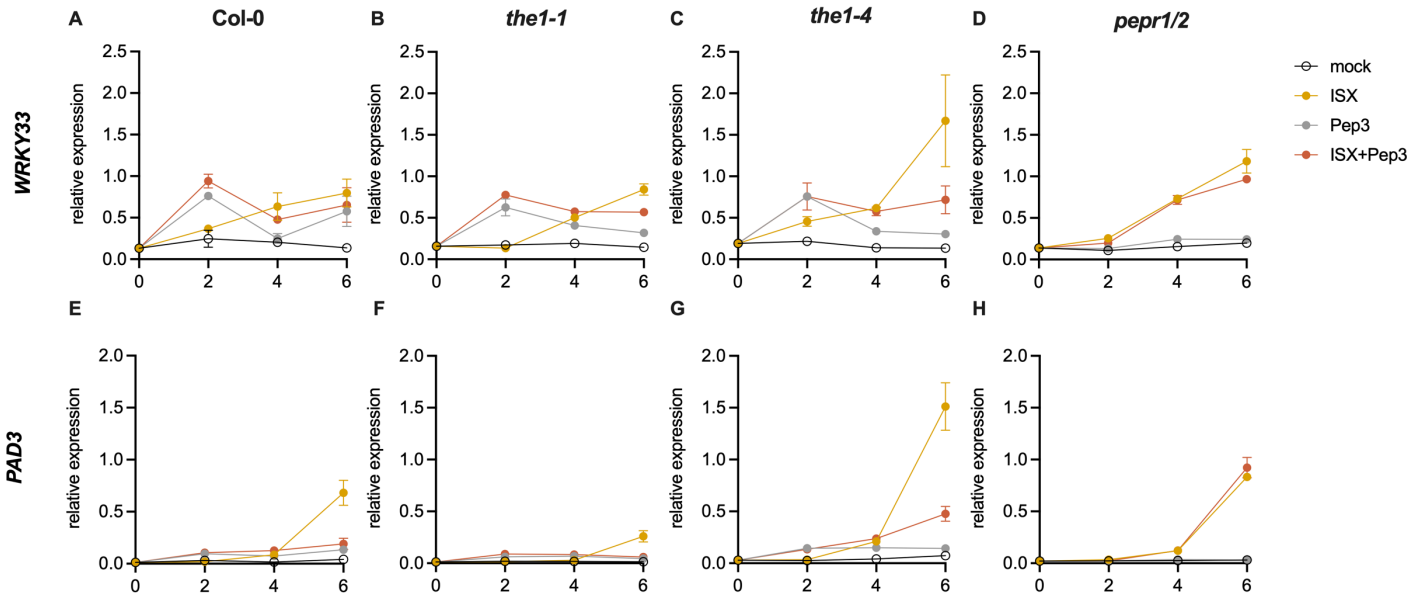

Figure S5: Time-course analysis of *WRKY33* and *PAD3* expression after Pep3 and ISX treatments. Relative expression of (A-D) *WRKY33* and (E-H) *PAD3* was determined in (A, E) Col-0, (B, F) *the1-1*, (C, G) *the1-4* and (D, H) *pepr1 pepr2* at 0, 2, 4 and 6 h after treatment with mock, Pep3, isoxaben (ISX) and ISX+Pep3 via quantitative RT-PCR. Values are relative to *ACT2* expression and error bars represent the SEM (n=3). Please note that the values for t = 4 h and 6 h are also shown in Figure 4 A-D.

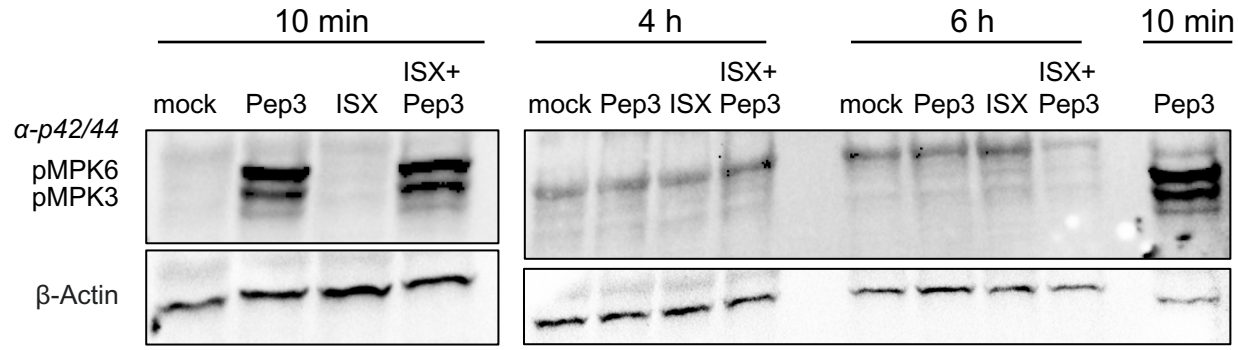

Figure S6: Investigation of MPK phosphorylation after ISX and Pep3 treatments.
Phosphorylation of MPK3 and MPK6 was determined in Col-0 seedlings at 10 min, 4 h and 6 h after treatment with mock, Pep3, isoxaben (ISX) and ISX+Pep3 by immunoblotting. Equal loading was checked with an anti-β-Actin antibody. Similar results were obtained in three biological replicates.

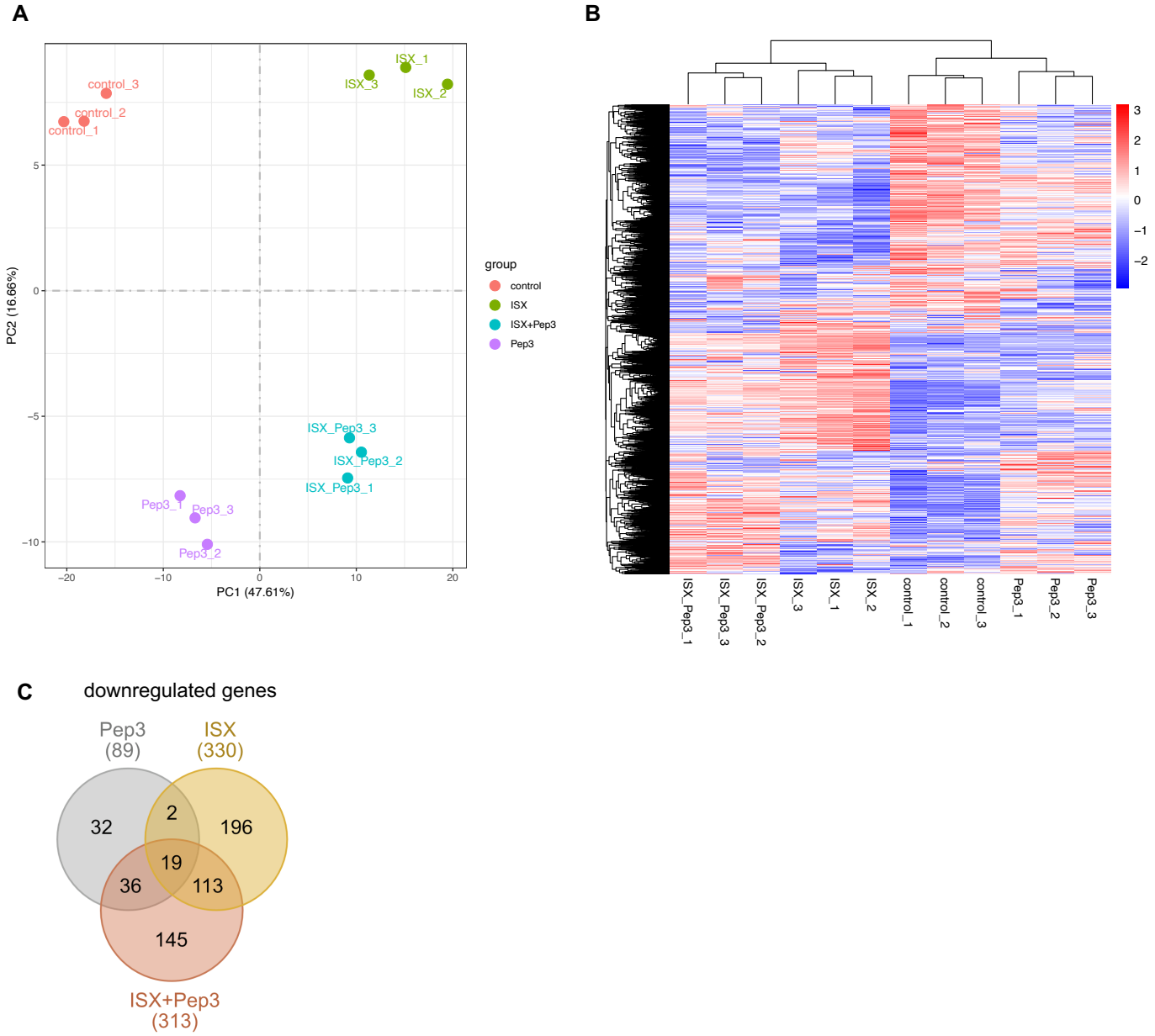

Figure S7: Principal component and hierarchical cluster analyses of RNA-Sequencing data. (A) Principal component analysis (PCA) of RNA-Sequencing data for Col-0 seedlings treated with mock, Pep3, isoxaben (ISX) and ISX+Pep3 for 6 h shows grouping of individual replicates (n=3) and main effects of treatments on gene expression. (B) Hierarchical cluster analysis displays similarities in gene expression after the different treatments and identifies sub-clusters. Heat map shows z-score of normalized data. (C) Significantly downregulated genes compared to mock treatment (α = 0.05, fold change >2).

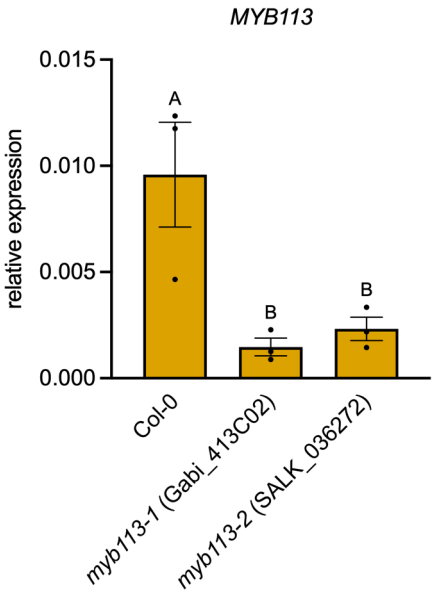

Figure S8: Genetic characterization of *myb113* mutants.
Relative expression of *MYB113* was determined in Col-0, *myb113-1* (Gabi_413C02) and *myb113-2* (SALK_036272) seedlings after 6 h treatment with isoxaben (ISX) via quantitative RT-PCR. Values are relative to *ACT2* expression and error bars represent the SEM (n=3). Different letters indicate statistically significant differences according to one-way ANOVA and Holm-Sidak's multiple comparisons test (α = 0.05).

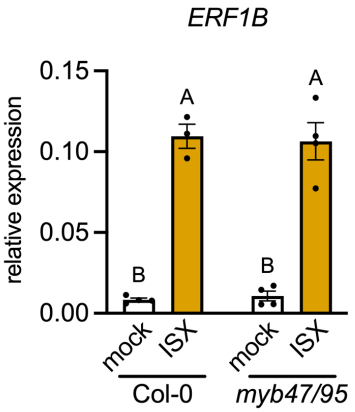

Figure S9: *MYB47* and *MYB95* do not affect *ERF1B* expression.
Relative expression of *ERF1B* was determined in Col-0 and *myb47/95* seedlings at 6 h after treatment with mock and isoxaben (ISX) via quantitative RT-PCR. Values are relative to *ACT2* expression and error bars represent the SEM (n=3). Different letters indicate statistically significant differences according to two-way ANOVA and Holm-Sidak's multiple comparisons test (α = 0.05).

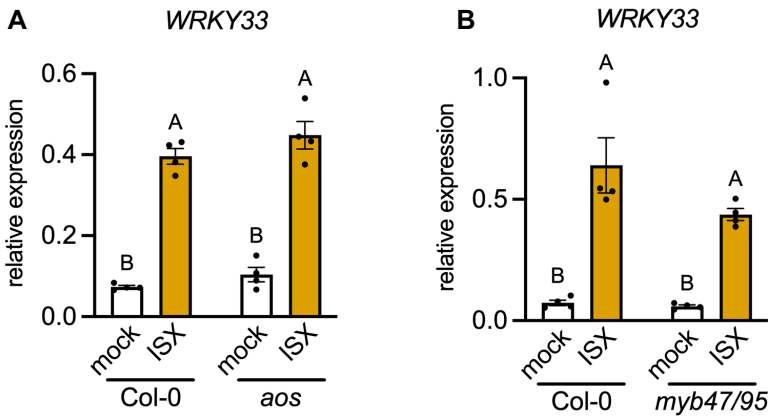

Figure S10: *WRKY33* expression does not require JA, *MYB47* or *MYB95*.
Relative expression of *WRKY33* was determined in (A) Col-0 and *aos* and (B) Col-0 and *myb47/95* seedlings at 6 h after treatment with mock and isoxaben (ISX) via quantitative RT-PCR. Values are relative to *ACT2* expression and error bars represent the SEM (n=3). Different letters indicate statistically significant differences according to two-way ANOVA and Holm-Sidak's multiple comparisons test (α = 0.05).

Supplemental Tables

Table S1. Arabidopsis genotypes used in this study.

Genotype	AGI	Stock code	Reference
the1-1	At5g54380	EMS mutant	Hematy et al., 2007
the1-4	At5g54380	SAIL_683_H03	Guo et al., 2009
pad3-1	At3g26830	EMS mutant	Glazebrook and Ausubel, 1994
the1-1 pad3-1	At5g54380, At3g26830	EMS mutant	Hematy et al., 2007, Glazebrook and Ausubel, 1994
cyp71a12	At2g30750	GABI_127H03	Millet et al., 2010
cyp71a13	At2g30770	SALK_105136	Nafisi et al., 2007
cyp71a12 cyp71a13	At2g30750, At2g30770	TALEN SALK_105136	Müller et al 2015
cas-1	At5g23060	SALK_070416	Weinl et al., 2008
mca1-null	At4g35920	n/a	Nakagawa et al., 2007
pepr1-1 pepr2-1	At1g73080, At1g17750	SALK_059281, SALK_036564	Yamaguchi et al., 2010
pec1-1 pec2-1	At5g02940, At5g43745	SAIL_300_A10, SALK_102200	Völkner et al., 2021
wrky33-2	At5g54380, At2g38470	GABI_324B11	Mao et al., 2011
the1-1 wrky33-2	At5g54380, At2g38470	EMS mutant, GABI_324B11	this study
the1-4 wrky33-2	At5g54380, At2g38470	SAIL_683_H03, GABI_324B11	this study
mpk3-1	At3g45640	SALK_151594	Ren et al., 2008
mpk6-3	At2g43790	SALK_127507	Liu and Zhang, 2004
pTHE1::THE1-GFP (the1-1)	At5g54380	n/a	Chaudhary et al., 2021
myb47-2	At1g18710	SALK_200360	Renard et al. 2020
myb47-1 myb95	At1g18710, At1g74430	SM_3_38234, GABI_314F05	Zhang et al., 2019
myb113-1	At1g66370	GABI_413C02	this study
myb113-2	At1g66370	SALK_036272	this study
aos	At5g42650	n/a	Park et al., 2002

Table S2. Primers used in this study.

Name	Method	Sequence (5'-3')	Reference
qWRKY33_fw	qRT-PCR	TAGAGCAAAGGAAGAACCAAACG	Schmidt et al., 2020
qWRKY33_rev		TGGTGGCAGAAATGTACAAAAGG	
PAD3_fw	qRT-PCR	TCGCTGGCATAACACTATGG	Giovannoni et al., 2021
PAD3_rev		TTGGGAGCAAGAGTGGAGT	
propep3_fw	qRT-PCR	CAACGATGGAGAATCTCAGA	Engelsdorf et al., 2018
propep3_rev		CTAATTGTGTTTGCCTCCTTT	
qJAZ10_fw	qRT-PCR	ATCCCGATTTCTCCGGTCCA	Gfeller et al., 2011
qJAZ10_rev		ACTTTCTCCTTGCGATGGGAAGA	
qWRKY67_fw	qRT-PCR	AAAGCCTCAGCGCACAAAAG	this study
qWRKY67_rev		TTGATCTTCTGCACCCGCTT	
MYB95_fw	qRT-PCR	TCTCCTACACCGAGCCCTAC	this study
MYB95_rev		GCGAGCTTGTTAAGGAAACG	
qMYB47_fw	qRT-PCR	GCTTACATCAACGAGCATGG	this study
qMYB47_rev		TCCACATCTCTGCAAACCAG	
MYB113_fw	qRT-PCR	TACTGGAGGCAGATGTGTTGG	this study
MYB113_rev		AAGTCAAGCGGTAAGGTCACA	
qERF1-fw	qRT-PCR	ATTCTTTCTCATCCTCTTCTTCT	Zhou et al., 2022
qERF1-rev		CGAATCTCTTATCTCCGCCG	
ACT2_q_for	qRT-PCR	CTTGCACCAAGCAGCATGAA	Czechowski et al., 2005
ACT2_q_rev		CCGATCCAGACACTGTACTTCCTT	